Advanced Materials Design Group amdg.science

Effects of texture on the functional and structural fatigue of a NiTi shape memory alloy

LePage W, Shaw JA, Daly SH

PUBLISHED AS

LePage W, Shaw JA, Daly SH. “Effects of texture on the functional and structural fatigue of a NiTi shape memory alloy.” International Journal of Solids and Structures 221, 150-164 (2021).

https://doi.org/10.1016/j.ijsolstr.2020.09.022

This is the accepted manuscript of an article published by Elsevier. The Version of Record is available at https://doi.org/10.1016/j.ijsolstr.2020.09.022.

LICENCE

This manuscript version is made available under the CC-BY-NC-ND 4.0 license (https://creativecommons.org/licenses/by-nc-nd/4.0/).

Self-archived by the authors in accordance with the publisher’s self-archiving policy. Provided for educational and personal use. Please cite the version of record.

ACCEPTED MANUSCRIPT · SELF-ARCHIVED AUTHOR VERSION

Graphical Abstract

Effects of Texture on the Functional and Structural Fatigue of a NiTi Shape Memory Alloy

William S. LePage, John A. Shaw, Samantha H. Daly

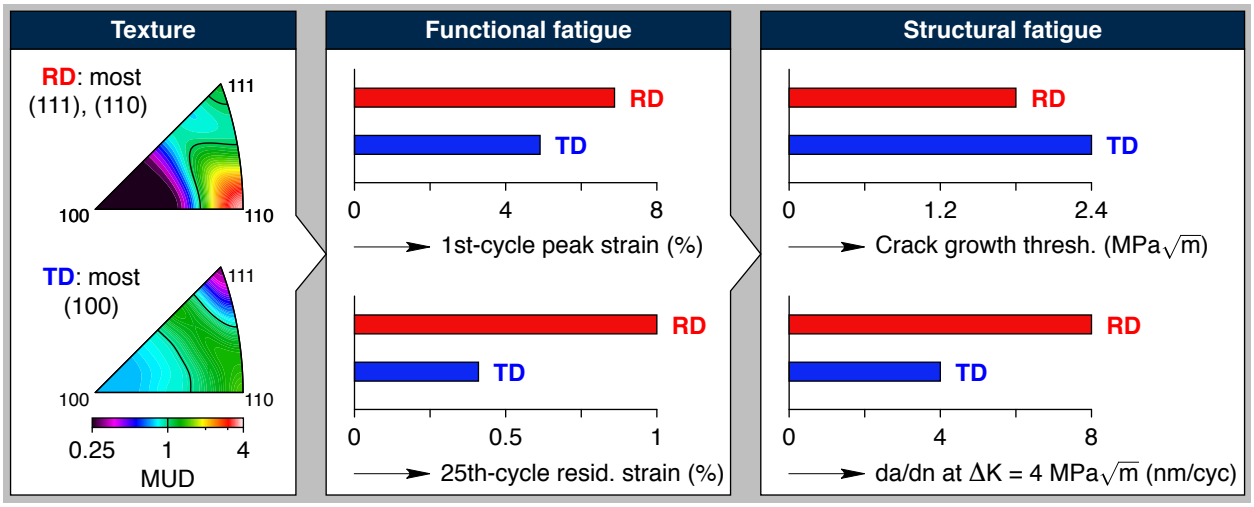

Highlights

Effects of Texture on the Functional and Structural Fatigue of a NiTi Shape Memory Alloy

William S. LePage, John A. Shaw, Samantha H. Daly

- Measured texture, functional fatigue, and structural fatigue from a NiTi sheet
- Twice as much plasticity accumulated for tension along the RD compared to the TD
- Cracks grew twice as fast in compact tension samples loaded along RD compared to TD
- Crack tip opened at a lower stress intensity when loaded in the RD than in the TD
- For less fatigue, plasticity resistance & A/M compat. override transformation strain

Effects of Texture on the Functional and Structural Fatigue of a NiTi Shape Memory Alloy

William S. LePage[a], John A. Shaw[b], Samantha H. Daly[c,*]

[a]*Department of Mechanical Engineering, University of Michigan, 2350 Hayward St., Ann Arbor, MI 48109, USA*
[b]*Department of Aerospace Engineering, University of Michigan, 1320 Beal Ave., Ann Arbor, MI 48109, USA*
[c]*Department of Mechanical Engineering, University of California, Santa Barbara, 2355 Engineering II, Santa Barbara, CA 93106, USA*

Abstract

The effects of crystallographic texture on the fatigue performance of superelastic NiTi sheet were investigated to assess the evolution of plastic deformation and transformation stress (functional fatigue) and the resistance to crack growth (structural fatigue). During uniaxial cycling, about twice as much plasticity accumulated for tensile specimens aligned in the rolling direction (RD) of the NiTi sheet compared to those in the transverse direction (TD). Fatigue experiments on compact tension specimens also showed a 25% lower fatigue threshold and twice the fatigue crack growth rate when loaded in the RD than in the TD. These macroscopic findings correlated with the microscopic observations of crack-tip displacements, where the crack tip opened at a lower stress intensity ($K \approx 0.9$ MPa$\sqrt{m}$) when loaded in the RD than in the TD (≈ 1.5 MPa$\sqrt{m}$). The dissimilar crack growth rates highlight the strong orientation-dependent mechanisms of plasticity, transformation, and twinning on both functional and structural fatigue. Although the RD had a larger transformation strain that might suggest an enhanced deformation accommodation, under stress-controlled cycling the TD was more resistant to plastic slip, leading to more reversible transformation. Assuming other microstructural aspects are held fixed (composition, grain size, and precipitates), these results suggest that tension along the textures akin to that of the TD (i.e., with a higher density of [1 0 0] and lower density of [1 1 1] and [1 1 0]) is beneficial to fatigue performance during stress-limited cycling.

Keywords: fatigue, shape memory alloys, texture

*Corresponding author
Email address: samdaly@engineering.ucsb.edu (Samantha H. Daly)

1. Introduction

Fatigue is a primary concern in NiTi research and development. One aspect of NiTi fatigue that remains unclear is the role of prevalent grain orientations, or crystallographic *texture*. Most NiTi product forms have strong texture that forms during processing. A significant body of work has investigated anisotropy and texture effects on the mechanical response of NiTi. Nonetheless, relatively few works have explored the influence of texture on the fatigue of NiTi.

Understanding and mitigating fatigue is important for a wide range of NiTi applications, ranging from biomedical devices, such as stents and root canal files [1], to lightweight wing actuators and planetary rover wheels [2]. Shape memory alloys (SMAs) undergo fatigue during mechanical and/or thermal cycling [3], and fatigue in SMAs can be classified in two types: structural or functional [4, 5]. Structural fatigue is common to engineering materials, and is principally concerned with the initiation and growth of cracks. Functional fatigue is characteristic of metals with reversible martensitic phase transformations, such as SMAs. Functional fatigue manifests from damage at the microscale. It involves not only conventional dislocation plasticity, but also other microstructural changes such as non-transforming ("locked-in") martensite and grain refinement [6, 7]. In uniaxial stress-strain responses during tensile cycling, functional fatigue is indicated by the gradual accumulation of residual strain ("ratcheting") and by the decrease in transformation plateau stress, transformation strain, and strain energy per cycle ("shakedown").

The fatigue of NiTi is complicated by dislocations that form during martensitic transformation. In the ideal case of perfect austenite-martensite compatibility, transformation occurs without persistent dislocations [8]. However, NiTi does not have perfect austenite-martensite compatibility. As a result, stress forms at the austenite-martensite interface and activates dislocations [9, 10]. Thus, phase transformation in NiTi is accompanied by dislocation networks that cause residual strain accumulation, locked-in martensite, and recurring patterns of martensite from cycle to cycle, both at the macroscale [11] and microscale [12].

Transformation and plasticity interact during the deformation of NiTi, and both are anisotropic. In terms of transformation, certain crystal orientations exhibit larger recoverable transformation strains. Specifically, as measured by experiments on single-crystal NiTi, transformation strains are largest near the $\langle 1\,1\,1 \rangle$ directions,[1] smallest for the $\langle 1\,0\,0 \rangle$ directions, and intermediate for the $\langle 1\,1\,0 \rangle$ directions [13–15]. In terms of plasticity, irreversible strains after unloading are largest during deformation along the $\langle 1\,1\,1 \rangle$ directions and smallest during

[1] Miller indices are given in the cubic basis for B2 austenite unless otherwise specified by subscript M for martensite.

deformation along the ⟨1 0 0⟩ directions [16–19]. Dislocation slip is suppressed in the ⟨1 0 0⟩ directions, owing to their unfavorable slip systems for dislocation flow in austenite [16].

As single-crystal NiTi is strongly anisotropic, a dominant texture in polycrystalline NiTi can substantially influence its mechanical response [20, 21]. In polycrystalline NiTi, different crystallographic textures form depending on the production process (e.g. drawing, swaging, rolling, and extruding) and heat treatment [22–26]. The drawing processes to create NiTi wire, bar, and tube typically result in a dominant (1 1 1) or (1 1 0) texture along the drawing direction [25, 27–29]. Similarly, rolled NiTi sheet has a dominant (1 1 1) or (1 1 0) texture in the rolling direction (RD) compared to the transverse direction (TD) [22, 25, 30–37].

Based on the slip and twinning systems of single-crystal NiTi, the typical texture of drawn wire or rolled sheet is particularly susceptible to plastic flow during tension along the drawing/rolling direction [14]. For example, after tensile load-unload cycles on polycrystalline NiTi sheets with (1 1 0) texture in the RD (similar to the texture of our sheet), the smallest residual strains were observed for tension along the TD [22, 37].

During martensitic transformation, texture in polycrystalline NiTi influences how martensite forms and evolves during deformation. Relative to the austenite lattice, a domain of martensite forms as one of 12 possible lattice correspondence variants (CVs). Calculations from measured lattice parameters for NiTi, however, have shown that the transformation strain of the martensite monoclinic lattice is not quite compatible with the austenite cubic lattice, so a perfectly coherent interface between austenite and a domain of a single martensite CV seems unlikely. Instead, two twin-related CVs in roughly 1/3 – 2/3 volume fractions can form to provide a compatible interface (habit plane) with austenite on average, taking one of 192 possible habit plane variants (HPVs) [38]. These still require some elastic (and intermittent plastic) accommodation at the interface, but it is minimal. If deformation persists, HPVs may detwin toward a single CV, but this requires increasing amounts of plastic slip near the austenite interface. Thus, while HPVs preserve an interface with austenite through fine twinning structures and an elastically deformed layer, single CVs (detwinned martensite) have a larger mismatch to be accommodated at the interface with austenite, presumably by irreversible plasticity. These issues are important for functional fatigue, as different configurations of martensite have a lower compatibility with the austenite and are associated with a higher dislocation density and residual strain.

Texture can affect the volume fraction of martensite, its twinning behavior, and the magnitude of its transformation strain [39]. Experimental works have investigated when and where specific martensite domains form in NiTi. Detwinning (into CVs) and twin nucleation (into HPVs) can occur simultaneously, as shown by recent microLaue diffraction measurements [40]. Furthermore, within individual grains, domains of untransformed austenite, HPVs (twinned

martensite), and single CV domains of martensite can coexist [12]. The degree of plasticity can vary locally within individual grains, as well. Upon unloading (after the first cycle), the largest residual strains were found at sites where high volume fractions of CVs had formed [12]. In terms of texture, this is important because deformation along the RD of a NiTi sheet forms about twice as much martensite into CVs (48%) compared to deformation along the TD (25%) [41]. Interestingly, texture does *not* influence the external work per unit volume to reorient martensite variants, as deduced from the product of plateau stress and recoverable shape-memory strain for samples with different textures [42].

In addition to its influence on functional fatigue, crystallographic texture changes the structural fatigue and fracture behavior of NiTi. The complex stress state in the vicinity of a crack tip is further complicated by the anisotropic behavior of NiTi in terms of transformation, plasticity, and twinning/detwinning. For example, in the high-stress region near a crack tip, transformation does not complete uniformly, as in-situ X-ray diffraction measurements revealed that some grains do not undergo $A \rightarrow M$ transformation [43]. In terms of fatigue crack initiation and growth, large (1 1 0) grains oriented along the tensile axis have the lowest fatigue resistance [44]. The role of anisotropy on detwinning can also be important for structural fatigue. Even in samples that begin with random orientations of martensite, high stress in the vicinity of a crack tip drives the preferential selection of CVs during detwinning [45]. Furthermore, twin boundaries can act as expedient paths for cracks. In a study of a NiTiHf SMA that used transmission electron microscopy [46], crack propagation followed a martensite band along the $\langle 1\,1\,0 \rangle_{\mathrm{M}}$ type II twin planes. The crack switched between twin planes to avoid Hf precipitates.

For conventional metals, increased ductility is associated with increased fracture toughness. However, experiments on single crystal NiTi [47] found that crystal directions with larger transformation strains exhibited a lower crack growth resistance. In particular, although a crystal with the [1 1 1] direction in tension exhibited more transformation and ductility, it had much less resistance to fracture during monotonic loading. While cracks grew in a stable manner in the [1 0 0] sample, unstable crack growth occurred in the [1 1 1] sample. Additionally, transformation in the [1 1 1] sample localized directly ahead of the crack tip, while transformation in the [1 0 0] sample localized to the sides of the crack tip. Transformation to the sides of the crack tip in the [1 0 0] sample was shown to dissipate more energy and promote stable crack growth.

While prior works have investigated the anisotropy and fatigue of polycrystalline and single-crystal NiTi, the connections among texture, functional fatigue, and structural fatigue remain unclear. In this work, functional fatigue was characterized by the accumulation of residual strain and the reduction in transformation stresses and strain energy during repeated load-unload cycles under uniaxial tension. Structural fatigue was probed through macroscale measurements of

fatigue crack growth rates, as well as microscale measurements of crack-tip displacements. When combined with measurements of texture from X-ray diffraction, these observations can be used to calibrate anisotropic models of fatigue in SMAs, guide material processing methods, and inform device designs.

2. Material and Methods

2.1. NiTi Sheet Material

All experiments in this work used samples cut from the same superelastic NiTi sheet. The sheet was 1 ± 0.08 mm thick of the "BB" alloy (50.8 at% Ni, lot 22180-100815), obtained from Memry Corporation (Hartford, CT). Per the manufacturer, the sheet was cold worked by rolling to approximately 30% thickness reduction, annealed in air with a hot-press furnace to heat treat and flatten the sheet, and chemically etched to remove rough surface oxides. Transformation temperatures were measured by differential scanning calorimetry (DSC) using a TA Instruments (New Castle, DE) Discovery DSC 2500 with a 3×3 mm specimen cut with a low-speed diamond saw. Figure S1[2] provides the DSC thermogram of the NiTi sample, showing an austenite finish temperature of 3 °C, consistent with the observed superelasticity at room temperature.

The grain size was characterized using transmission scanning electron microscopy (TSEM). For as-received NiTi with cold working, like the current sheet material, the grain sizes are generally too small for electron backscatter diffraction (EBSD). A foil sample was prepared with focused-ion beam (FIB) liftout in SEM, with its surface normal parallel to the rolling direction of the sheet. Using TSEM, grain sizes on the order of 20 to 200 nm were observed (Figure S2). The sample region that had sufficient electron transparency for TSEM was relatively small, so larger grains may also have been present in the foil.

Crystallographic texture was characterized with X-ray diffraction (XRD). For XRD measurements, a 20×20 mm piece of the sheet material was cut by a low-speed diamond saw, then ground and polished with a progression of 600, 800, and 1200 grit silica papers with flowing water. The final polishing step to a mirror finish was performed with a 5:1 volume-ratio mixture of colloidal silica (Buehler MasterMet 2, 0.02 μm) and 30% hydrogen peroxide (Fisher H325) on a microfiber cloth (Buehler MicroCut). In-plane pole figures were measured with a Rigaku SmartLab XRD for the (1 1 0), (2 1 1), and (2 0 0) poles of both the sheet material and a powder sample (B2 $Ni_{51}Ti_{49}$ powder from Special Metals, New Hartford, NY). The powder sample, with a presumably uniform texture, was used as a control sample to correct the sheet measurements for attenuated reflections due to tilting during the in-plane measurements (defocusing). The XRD

[2]References to Supplementary Material are denoted by a prefixed "S".

used a copper anode at 40 kV and 44 mA, parallel beam (PB) collimator slit, 0.5° in-plane parallel slit collimator (PSC), 10 mm length limiting slit, and a 0.5° in-plane parallel slit analyzer (PSA). The attenuator was open, the divergence slit was 1 mm, and the Soller and receiving slits were 2 mm.

The orientation distribution function (ODF) of the sheet's texture was calculated from the corrected in-plane pole figures. The ODF assumed orthorhombic sample symmetry, and the data was fitted with the MTEX open source Matlab toolbox [48]. The ODF was plotted with respect to the sheet's normal direction (ND), rolling direction (RD), 45° from the rolling direction, and transverse direction (TD). Pole figure (PF) measurements, the fitted orientation distribution function (ODF), and the error between the PF and ODF are provided in Figure S4. Significant texture was observed in both the RD and TD of the sheet, with several regions having about 10 multiples of uniform distribution (MUD).

The inverse pole figures (IPFs) of Figure 1 show that the RD had about 3× as many [1 1 1] directions compared to the TD. The strongest texture among the RD, 45, and TD sheet directions was (1 1 0) in the RD, with 3.7 MUD. However, the strongest texture in the IPFs was (1 1 1) in the normal direction (ND) with 9.4 MUD. The (1 1 1)||ND texture is commonly called the γ-fiber texture, and it is characteristic of rolled sheets of BCC metals [49], as well as austenite B2 NiTi [32, 34–36, 50]. When the orientation distribution function was visualized as ϕ_2 slices (Figure S6), there was a clear γ-fiber texture, with a region having MUD >> 1 along the (1 1 1) plane normal in the $\phi_2 = 45°$ slice. The two local maxima of the orientation density were at $(1\,1\,1)[1\,\bar{1}\,0]$ and $(1\,1\,1)[0\,\bar{1}\,1]$, so we classify our NiTi sheet as predominantly a $\{1\,1\,1\}\langle 1\,\bar{1}\,0\rangle$ texture (ND parallel to plane normals {1 1 1} and RD parallel to directions $\langle 1\,\bar{1}\,0\rangle$).

2.2. Experimental Setup and Procedures

Three types of mechanical experiments were performed to study the influence of texture on the mechanical behavior of superelastic NiTi. The first type consisted of uniaxial tension experiments on tensile samples. The second type consisted of fatigue crack growth experiments on notched compact tension samples. The third type consisted of microscopic measurements of crack opening and strain fields near the crack tip in precracked compact tension samples. Experiments were performed on new samples (except for the third type) with three different texture orientations in room temperature air. Optical digital image correlation (DIC) was used in the first two experiment types, and SEM-DIC was used in the third type. Sample preparation methods and experiment procedures for each type of experiment are provided below.

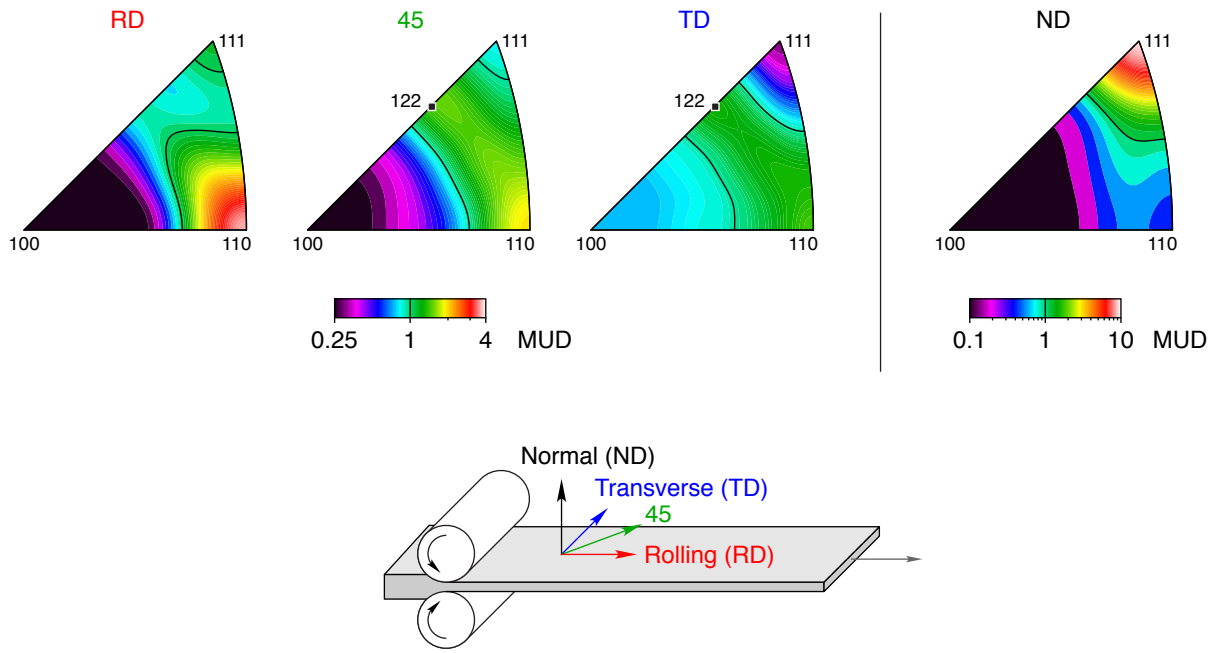

Figure 1: Significant crystallographic texture was present in the NiTi sheet. Inverse pole figures (IPFs) are shown for the sheet's rolling direction (RD), 45° from the rolling direction (45), transverse direction (TD), and normal direction (ND). For clarity, the IPFs for RD, 45, and TD have a different contour scale than the ND IPF. The strongest texture in the IPFs was (1 1 1) in the normal direction (9.4 MUD). The strongest texture in the IPFs in the plane of the sheet was (1 1 0) in the rolling direction (3.7 MUD).

2.2.1. Uniaxial Tension

Dogbone-shape tension samples with dimensions shown in Figure 2a were wire-electrodischarge machined (EDM) from the NiTi sheet. Tensile samples of three texture orientations (RD, 45, and TD) were used in the cyclic tension experiments of Section 3.2. These tension tests (Section 3.1) were performed in a 200 kN mechanical testing system (Instron 5585; Norwood, MA) equipped with a 5 kN Instron load cell (Figure S7). The samples were loaded in displacement control with a constant nominal strain rate of $\pm 1 \times 10^{-4}$ s^{-1} for 25 load-unload cycles. The nominal stress in the gauge section (σ) was measured from the global force (P) and initial area (A_0), with $\sigma = P/A_0$. The cycle limits were $\sigma = 450$ MPa on loading and $\sigma = 4.5$ MPa on unloading. Stress (load) limits were chosen, instead of strain (elongation) limits, for consistency with the other crack growth experiments that were cycled to a prescribed stress intensity (load) limit.

The average engineering strain (ε) in the gauge section was measured by a DIC virtual extensometer. It measured the change in length (δ_e) of the narrow region of the dogbone (initial

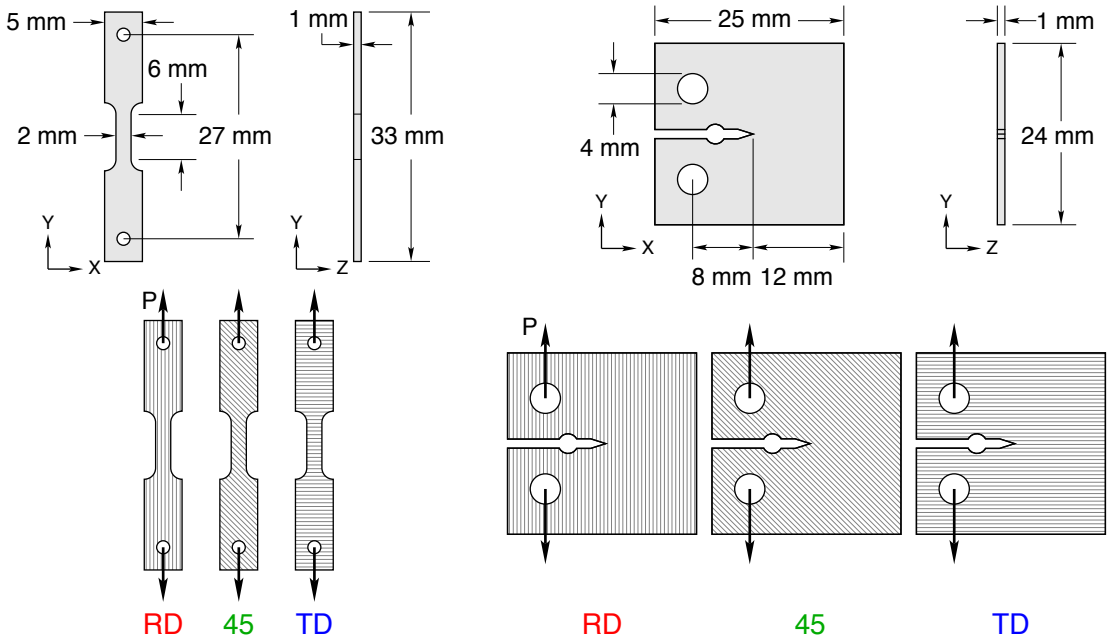

(a) Tension samples

(b) Compact tension samples

Figure 2: Samples for uniaxial tension (a) and fatigue crack growth (b) experiments were cut from the NiTi sheet. Three different texture directions were produced: tensile axis (Y) parallel to the sheet rolling direction (RD), tensile axis 45° from the sheet rolling direction (45), and tensile axis perpendicular to the sample rolling direction (TD).

length $L_e = 6$ mm) to give the axial strain $\varepsilon = \delta_e/L_e$. The residual strain ($\varepsilon_r$) was measured at the minimum stress at the completion of each cycle (4.5 MPa).

Full-field displacements on the surface of the sample were measured with an optical 3-D digital image correlation (DIC) system comprised of two cameras (PointGrey GRAS 50S5M-C) with lenses (Nikon Nikkor 200 mm, f/16), and two LED lights (Genaray MonoBright). To improve accuracy, the DIC setup utilized cross polarization between the lenses and lights to eliminate saturated pixels and increase contrast [51]. A gently blowing fan was placed approximately 1 m from the side of the sample to avoid heat wave distortions from the high-intensity lights [52]. The samples were speckle patterned using an airbrush (Iwata CM-B) with a basecoat of white paint (Golden High Flow Titanium White, no. 8549-4, lot 366162) followed by a speckle pattern of black paint (Golden High Flow Carbon Black, no. 8040-4, lot 345307). This paint sequence provides greater contrast and less error than the converse [53]. The optical 3-D DIC images were correlated with Vic3D 7 software with low-pass filtering, Gaussian subset weights, eight-tap interpolation, and the normalized squared differences method. The

correlation thresholds were 0.02 px consistency threshold, 0.05 px maximum correlation confidence interval (CCI), and 0.1 px matchability. These same correlation parameters were also used in the fatigue crack growth setup below.

2.2.2. *Fatigue Crack Growth*

Compact tension (CT) samples with dimensions shown in Figure 2b, following ASTM E561 [54], were wire-electrodischarge machined (EDM) from the same NiTi sheet as the tension samples. The perpendicular distance between the applied loads (P) and the notch was $a_0 = 8$ mm. Samples with three different texture orientations (RD, 45, and TD) were used in the fatigue crack growth experiments of Section 3.2. Prior to the experiments, compact tension samples were prepared by polishing to a mirror finish, suitable for subsequent microscopic measurements. The same grinding and polishing procedure as the XRD sample described in Section 2.1 was used. The compact tension sample was relatively thin ($\approx$ 1 mm) compared to the in-plane dimensions ($\approx$ 24 mm), so the loading was nominally plane stress. The crack growth experiments were performed in an electrodynamic voice-coil fatigue system (ElectroForce LM1, 220 N dynamic cycling capacity, TA Instruments).

The nominal stress intensity (K) was calculated following ASTM E561 11.3 [54] (same as in [55]). This calculation was based on linear-elastic fracture mechanics (LEFM) which assumes a small inelastic zone at the crack tip. Recently, the effective stress intensity for cracks in SMAs was shown to differ from those predicted by LEFM, since the elastic moduli of austenite and various configurations of martensite differ considerably and are all are strongly anisotropic [56–59]. Nevertheless, the nominal LEFM stress intensity was used here as a basic measure of stress intensity that is proportional to the applied load. The load ratio for all fatigue cycles was $P_{min}/P_{max} = 0.1$, which in the linear elastic fracture regime is the equivalent to $R = K_{min}/K_{max} = 0.1$.

Fatigue cracking experiments were performed in two regimes, one at a high stress intensity amplitude ($\Delta K = K_{max} - K_{min}$) and another at a low stress intensity amplitude. Fatigue cycling was started at a relatively high value ($\Delta K_0 = 6.4$ MPa $\sqrt{m}$) to initiate and study crack propagation at relatively fast crack growth rates. Once the crack grew about 2 mm from the notch in the CT specimen ($a = 10$ mm), the fatigue threshold (ΔK_{th}) was determined. This was done by incrementally reducing the stress intensity amplitude by 0.2 MPa $\sqrt{m}$ until the average crack growth rate during at least 50,000 cycles was slower than one Angstrom per cycle (10^{-10} m/cycle). After the fatigue threshold was measured, crack growth was allowed to proceed, starting at a relatively low stress intensity amplitude (typically $\Delta K < 3$ MPa $\sqrt{m}$). The cyclic rates for the high and low stress intensity regimes were 10 Hz and 50 Hz, respectively.

Crack growth rates were measured by optical 3-D DIC. Images were captured at selected

cycling intervals (e.g. every 1,000 fatigue cycles during high ΔK experiments) during 1 second pauses at the minimum and maximum cyclic force. The crack-tip position was measured from the DIC images using either the correlation confidence interval (CCI) for the experiments with $\Delta K \geq 6.4$ MPa $\sqrt{m}$, or the normal strain (ε_{YY}) for $\Delta K < 6.4$ MPa $\sqrt{m}$. Strain can indicate crack tip position for brittle materials, such as concrete [60], or for ductile materials at relatively low stress intensities. At relatively high stress intensities, however, the strain in front of the crack tip can be large enough that normal strain is no longer a reliable measure of crack tip position. However, as a crack opens, subsets that span the crack have poorer correlation, which is reflected as an increase in CCI [61, 62]. In the present work, at relatively high stress intensities, the CCI at a threshold of 0.005 to 0.009 px was used to detect the crack tip position. At relatively low stress intensities, the increase in CCI was negligible, so ε_{YY} at a threshold of 0.4% to 0.8% strain was used to detect the crack tip position. Although the crack is usually manually removed from the area of interest (AOI) in DIC measurements due to poor correlation across the crack faces, our crack-tip location methods kept the crack in the DIC AOI. Further details of this method are outlined in [55].

2.2.3. Microscopic Measurements

Microscopic deformations near the crack tip were measured with digital image correlation in a scanning electron microscope (SEM-DIC) [63, 64]. Compact tension samples (one each RD, 45, and TD) that were previously subjected to crack growth experiments were subjected to an additional load-unload experiment within the SEM (3.3). After the crack growth experiment, the painted speckle pattern for optical DIC was removed with methanol, and the samples were re-polished (5:1 volume ratio mixture of colloidal silica and hydrogen peroxide) and speckle patterned with Au nanoparticles for SEM-DIC. The method followed [65] with the following exceptions: (1) instead of hydroxylation in a base, the final polishing step with hydrogen peroxide and colloidal silica provided sufficient hydroxyl groups on the sample surface for silanization; (2) instead of 24 hours for silanization, only 4 hours were needed; and (3) instead of fabricating Au nanoparticles following the method of Frens [66], commercially-obtained Au nanoparticles were applied (250 nm, in 0.1 mg/mL sodium citrate with stabilizer; Alfa Aesar, Ward Hill, MA).

After Au nanoparticle patterning, the compact tension samples were loaded in a Kammrath and Weiss (Dortmund, Germany) in-SEM 10 kN capacity tension/compression stage equipped with 500 N load cell (Figure S9). The in-situ stage was operated in a field-emission gun SEM (Teneo; Thermo Fisher Scientific, formerly FEI). The beam conditions were 30 kV and 0.8 nA, with a working distance of 18 mm. Images were recorded in the SEM, which was equipped with a custom scan controller that significantly reduced the scanning errors that are problematic for SEM-DIC [67]. This method was able to capture the < 20 nm differences in crack separations between

the three sample textures. The scan controller was programmed to raster "out and back" along the same line of pixels and average these two scan lines for each line in the image. The effective dwell time was 6.4 µs per pixel. The images were 300×300 µm and 4096×4096 px, resulting in a pixel size of 73 nm.

The micrographs for SEM-DIC measurements were correlated using Vic2D 6 software with low-pass filtering, Gaussian subset weights, eight-tap interpolation, and the normalized squared differences method. The correlation thresholds were 0.02 px consistency threshold, 0.05 px maximum confidence interval, and 0.1 px matchability (the same as for optical DIC).

3. Experimental Results

3.1. Uniaxial Cyclic Tension Results

The texture-dependent functional fatigue was examined for 25 load-unload cycles of the superelastic NiTi under uniaxial tension (Figure 3). All three sample textures (RD, 45, and TD) exhibited the typical tensile response of superelastic NiTi, with an initial elastic loading of austenite up to about 0.5% strain, followed by a nucleation peak during the localization of $A \rightarrow M$ phase transformation. Subsequently, phase transformation propagated along the sample during the stress plateau (Figure 3a). During the first cycle ($n = 1$), the stress plateau on loading ($A \rightarrow M$) was highest for TD (415 MPa) and lowest for RD (337 MPa). The stress plateau for the 45 texture was approximately the average of those for RD and TD (380 MPa). After 25 cycles, the differences between the loading plateaus became more pronounced. Phase front propagation completed at $\varepsilon \approx 4\%$ strain for the TD sample, compared to $\varepsilon \approx 6\%$ strain for the RD sample (Figure 3a). At these points the stress plateau ended, and the response stiffened. During the final cycle ($n = 25$), the TD sample no longer had a flat stress plateau on loading; whereas, the RD sample continued to exhibit flat stress plateaus during loading for all 25 cycles.

The TD sample exhibited the lowest shakedown rate of the plateau stress (Figure 3b). For each cycle, the loading plateau stress (σ_p, indicated by markers in Figure 3a) was selected from the point on the response curve at a strain equal to half of the cycle's maximum strain. Averaged over the 25 cycles, the plateau stress decreased at 2.9 MPa/cycle for TD, compared to 3.2 MPa/cycle for 45 and RD.

To estimate the asymptotic behavior of the cyclic responses, a simple exponential function was used to fit the plateau stresses on loading (σ_p) and the residual strains (ε_r),

$$F(n) = B_1 - B_2 \exp\left(-n/B_3\right). \tag{1}$$

where (B_1, B_2, B_3) were fitting parameters. Although Equation (1) has no physical basis for the evolution of σ_p or ε_r, it correlated well with both. The coefficients of determination (R^2) were

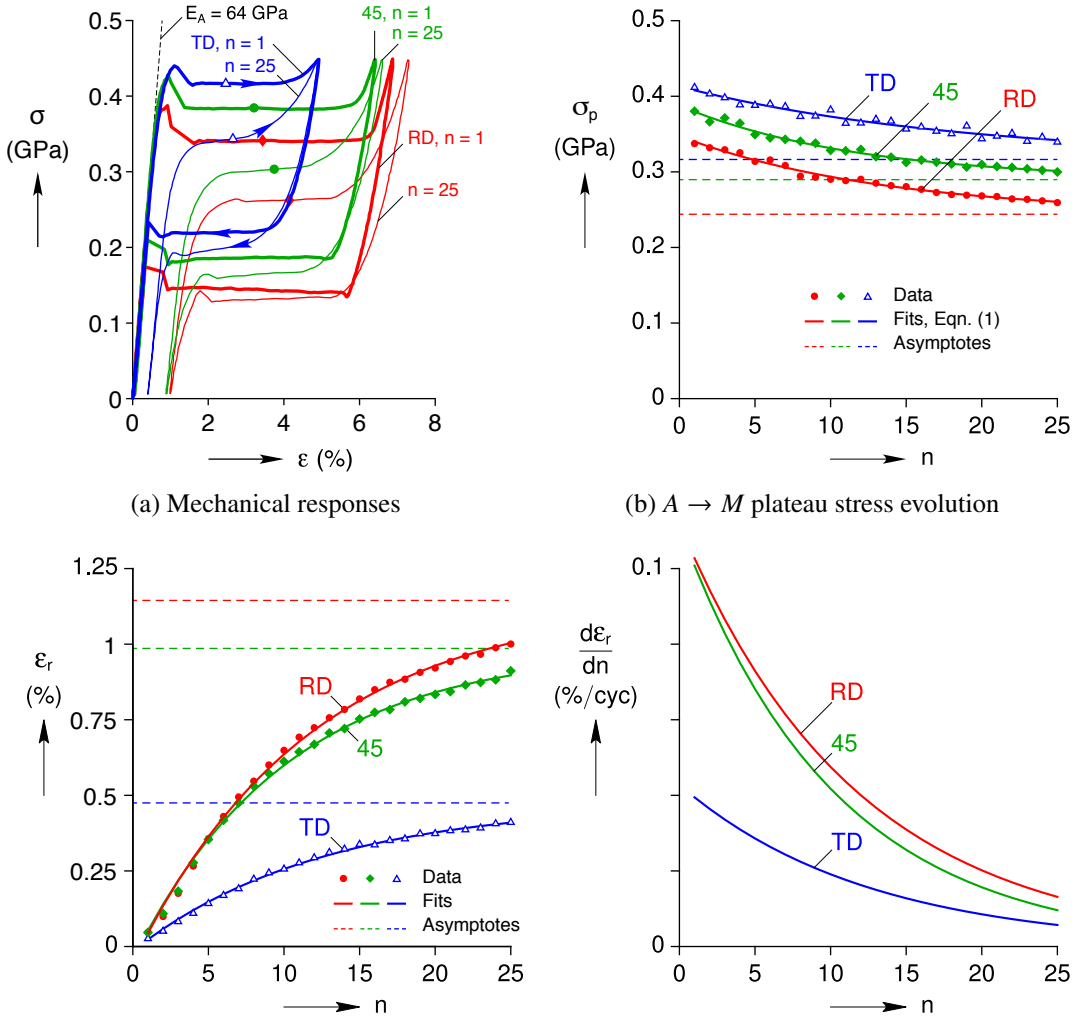

(a) Mechanical responses

(b) $A \rightarrow M$ plateau stress evolution

(c) Residual strain evolution

(d) Cyclic rate of residual strain

Figure 3: Uniaxial tension cycling results for RD, 45, and TD textures: (a) Mechanical responses during the first and 25th cycles with plateau stresses (σ_p) during loading ($A \rightarrow M$) indicated by markers. (b) The evolution of plateau stress (σ_p) with cycle number (n). (c) The evolution of residual strain (ε_r) with cycling. (d) The rate of residual strain accumulation ($d\varepsilon_r/dn$) with cycling, computed from the residual strain fits.

greater than 0.951 for the loading plateau stresses (Table SI) and greater than 0.997 for the residual strains (Table SII). To extrapolate beyond 25 cycles, the limiting value is $\lim_{n\to\infty} F(n) = B_1$. The asymptotes of σ_p were $B_1 = 0.244$ GPa (RD), 0.290 GPa (45), and 0.316 GPa (TD), as shown by dashed lines in Figure 3b. All the fitting parameters are tabulated in Table SI.

After 25 cycles, the TD sample accumulated about half as much residual strain as the RD and

45 samples (Figure 3c). Extrapolating the asymptotes of the fits to $n \to \infty$, TD had about half of the residual strain (0.48%) compared to RD (1.15%), while 45 was comparable to RD (0.99%). The rate of residual strain accumulation per cycle ($d\varepsilon_r/dn$) was calculated from the derivative of the fit function (Figure 3d). For RD and 45, $d\varepsilon_r/dn$ was about 0.1%/cycle at $n = 1$, while the value for TD was much lower, at about 0.04%/cycle. By $n = 25$, the residual strain accumulation rate was small, $d\varepsilon_r/dn < 0.02\%$/cycle for all samples. Also, emphasizing the trends noted above, it is interesting that the maximum strain (at 450 GPa) increased noticeably (by about 0.4% strain) during cycling for the RD sample, less so (about 0.17%) for the 45 sample, but not at all for the TD sample Figure 3a.

During the tension cycles, the RD and 45 samples dissipated more energy than the TD sample. For each cycle, the density of mechanical work ($W = \int \sigma\dot{\varepsilon}\, dt$) done on the sample was calculated separately for loading ($W^+ > 0$) and unloading ($W^- < 0$), and the energy lost, or net work done, was calculated from $W_{net} = W^+ + W^-$ (see Figure 4). The work during loading (W^+) was about the same for RD and 45 samples across all cycles, and both were larger than that for the TD sample. They all trended downward (nearly) monotonically with cycling. The recovered work during unloading ($-W^-$) was only slightly different among the three cases, with a slightly larger magnitude (interestingly) observed in the 45 sample. In all cases, W^- did not change much with cycling, especially in the TD sample. The energy lost (W_{net}) largely followed the trends of W^+, with a gentle downward progression with cycling, except that the 45 sample now appeared at intermediate values between the RD (although quite close) and the TD sample. This was consistent with the area within the first cycle loops in Figure 3a, all with a stress hysteresis about 200 MPa but successively decreasing plateau strains in RD, 45, and TD. In any event, the RD and 45 samples dissipated more energy than the TD sample, and the difference was especially apparent in the first four cycles. At cycle 25, W_{net} = 6.89, 6.47, and 4.95 MJ/m^3 for RD, 45, and TD, respectively.

In addition, the strain fields measured by DIC showed interesting differences between the sample textures in their transformation morphologies, which would not be apparent in their strain-averaged structural responses. Figure 5 shows sequences of color contour plots of the axial strain field $\varepsilon_{YY}(X, Y)$ during selected cycles (n = 1, 2, 3, 5, 10, 15, and 25) for each sample texture (row). These are grouped in two columns to show time instances during the onset of $A \to M$ localization (start of the loading plateau) and the final $M \to A$ coalescence (end of the unloading plateau), denoted for each cycle n^+ and n^-, respectively. While macroscopic strain *localization* and *coalescence* stayed in the same location from cycle to cycle for RD and 45 (consistent with prior work [11]), these features appeared in seemingly random locations for TD. One reason for this may be the higher density of [1 0 0] in TD (0.8 MUD) compared to that of RD and 45 (0.3 MUD), as X-ray diffraction measurements have shown that [1 0 0] grains can redirect or stall

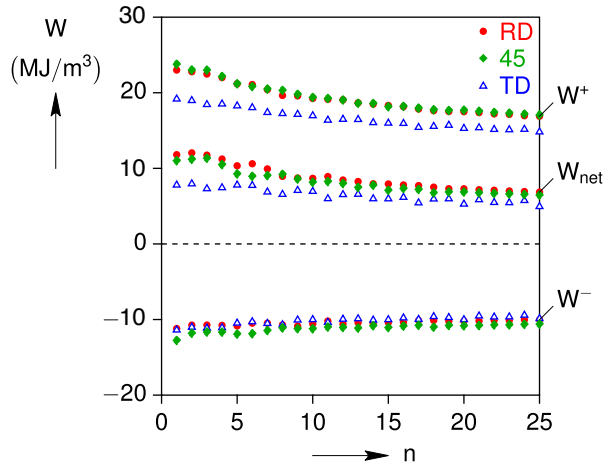

Figure 4: The evolution of mechanical work density for the three sample textures during 25 load-unload cycles, with positive work during loading (W^+), negative during unloading (W^-), and the net work, $W_{\text{net}} = W^+ + W^-$.

martensite fronts [68]. In the later cycles, localizations were progressively less narrow and distinct for all three textures, especially TD where localization was largely absent by $n = 10^+$ during $A \rightarrow M$.

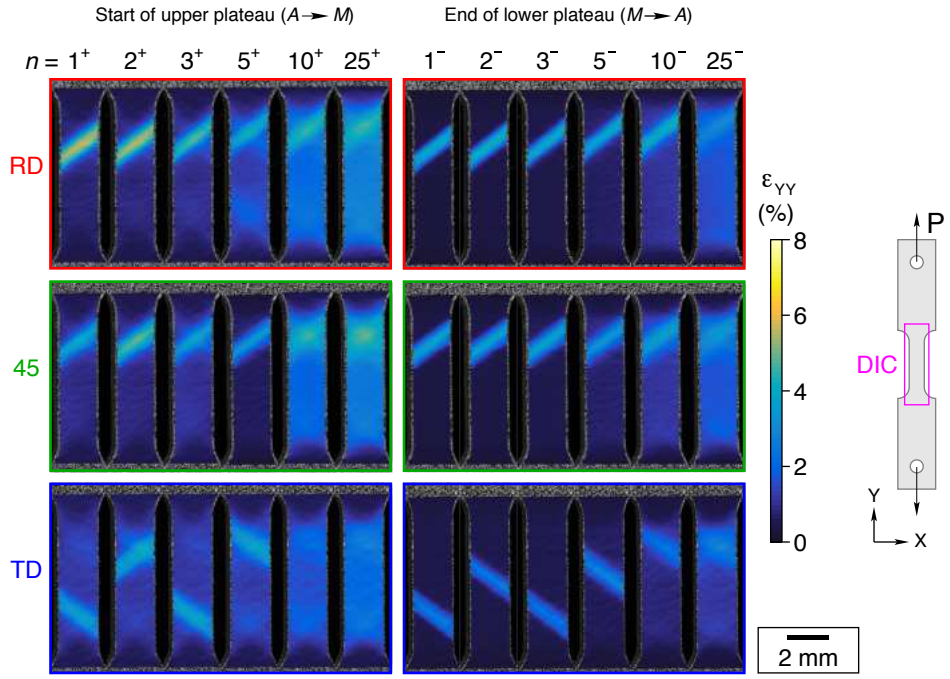

Figure 5: Maps of axial Lagrangian strain (ε_{YY}) from the 3-D DIC images nearest the macroscopic nucleation and coalescence of phase transformation for n = 1, 2, 3, 5, 10, and 25, during loading (n^+) and unloading (n^-).

3.2. Fatigue Crack Growth Results

Fatigue crack growth experiments were performed on each texture (RD, 45, TD) using compact tension samples. A total of nine experiments (three samples from each texture) were done at relatively high stress intensity amplitude (ΔK) over roughly 10^5 cycles, while monitoring the evolving crack length a. One sample from each group was then subjected to additional cycling (roughly 10^6 cycles) at a low stress intensity amplitude to asses the high cycle fatigue behavior and to quantify the threshold stress intensity (ΔK_{th}).

As mentioned previously, macroscopic crack growth was measured by optical DIC in two ways: either by the correlation confidence interval (CCI) for the high ΔK experiments or by the maximum principal strain for the low ΔK experiments. To illustrate the efficacy of DIC for tracking crack tips in the former case, Figure 6 shows an example for each sample texture of the crack path at the end of a high ΔK crack growth experiment. Each case includes a contour plot of the CCI field, a micrograph by optical microscopy (after the speckle pattern was removed), and a semi-transparent overlay of the micrograph on the CCI field in a magnified view near the crack tip. As expected for DIC, the CCI was rather high in the neighborhood of the crack face. This is seen in Figure 6 as the mostly yellow regions (CCI $\approx$ 0.009 px), but with some dark islands where the CCI threshold of

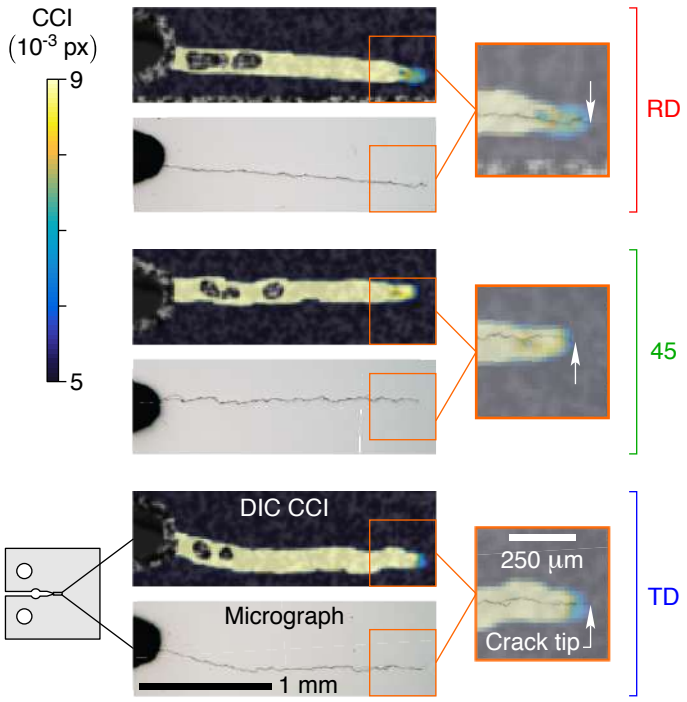

Figure 6: Crack-tip locations were measured by the DIC correlation confidence interval (CCI) in the high stress intensity crack growth experiments. An example is shown for each sample texture at the end of its experiment, consisting of a CCI field, an optical micrograph of the entire crack (after the speckle pattern had been removed), and a magnified view near the crack tip with a semi-transparent overlay of the micrograph on the CCI field. The apex of the steep gradient in the CCI field was quite effective in locating the crack tip (within ±25 μm).

0.050 px was exceeded. The DIC software considered those points uncorrelated and removed them from the field. Everywhere else, however, the CCI was quite low (< 0.005 px), and the correlation was strong. The magnified overlay showed steep gradients in the CCI around the crack tip, and the 'nose' of this region aligned nicely with the micrograph of the crack in each case. The region of elevated CCI captured the final position of the crack tips to within ±25 μm, as compared to the corresponding optical micrographs.

The results from all crack growth experiments are provided in Figure 7, indicating generally faster crack growth in the RD samples than in the 45 and TD samples. All experiments began with an initial crack length of $a_0 = 8$ mm (CT notch depth to the load) and an initial stress intensity amplitude of $\Delta K_0 = 6.4$ MPa $\sqrt{\text{m}}$. Figure 7a shows the evolution of the crack length (a) with cycle number (n), and the crack growth rates are plotted in Figure 7b in terms of the crack extension per cycle da/dn versus the increasing ΔK (as a increased during each experiment). The crack growth in the RD samples generally outpaced all the others, and the cracks in the TD samples

grew uniformly slowly. (The three cases in Figure 7b labelled with asterisks were the samples used in subsequent microscopic crack measurements in Section 3.3.) The 45 samples exhibited a wider variability than the others, and one exhibited the slowest crack growth of all. This outlier, denoted '45 (bifurc.)' in Figures 7a and 7b, was traced to the unusual formation of a bifurcated crack. This bifurcation is shown in Figure S10, where the initial crack arrested after about 250 μm of extension, and then a second crack dominated the remainder of the fatigue crack growth. This underlies the value of using full-field tracking methods like DIC to capture the details of fatigue crack growth morphology.

One sample of each texture was subjected to further cycling, starting at a low ΔK, as shown in Figures 7c and 7d. While it might appear in Figure 7c that the fatigue crack in the TD sample grew faster than the others, it had a head start with a slightly longer initial crack for this segment of cycling. The plot in Figure 7d accounts for the larger starting ΔK, and clearly shows that the RD sample had a much faster crack growth rate per cycle than 45 or TD (which were similar). For example, at $\Delta K = 3$ MPa $\sqrt{\text{m}}$, the crack growth rate in RD sample was 3×10^{-9} m/cycle, twice as fast as that of the 45 and TD samples. The Paris law with an exponent of 3 is shown for reference by the gray dashed line, and all cases reasonably follow this slope. The plot also shows a lower fatigue threshold for the RD texture ($\Delta K_{th} = 1.8$ MPa $\sqrt{\text{m}}$) compared to 45 and TD (both $\Delta K_{th} = 2.4$ MPa $\sqrt{\text{m}}$). These fatigue thresholds agree with previous fatigue cycling measurements on superelastic NiTi with a stress ratio of $R = 0.1$ [69].

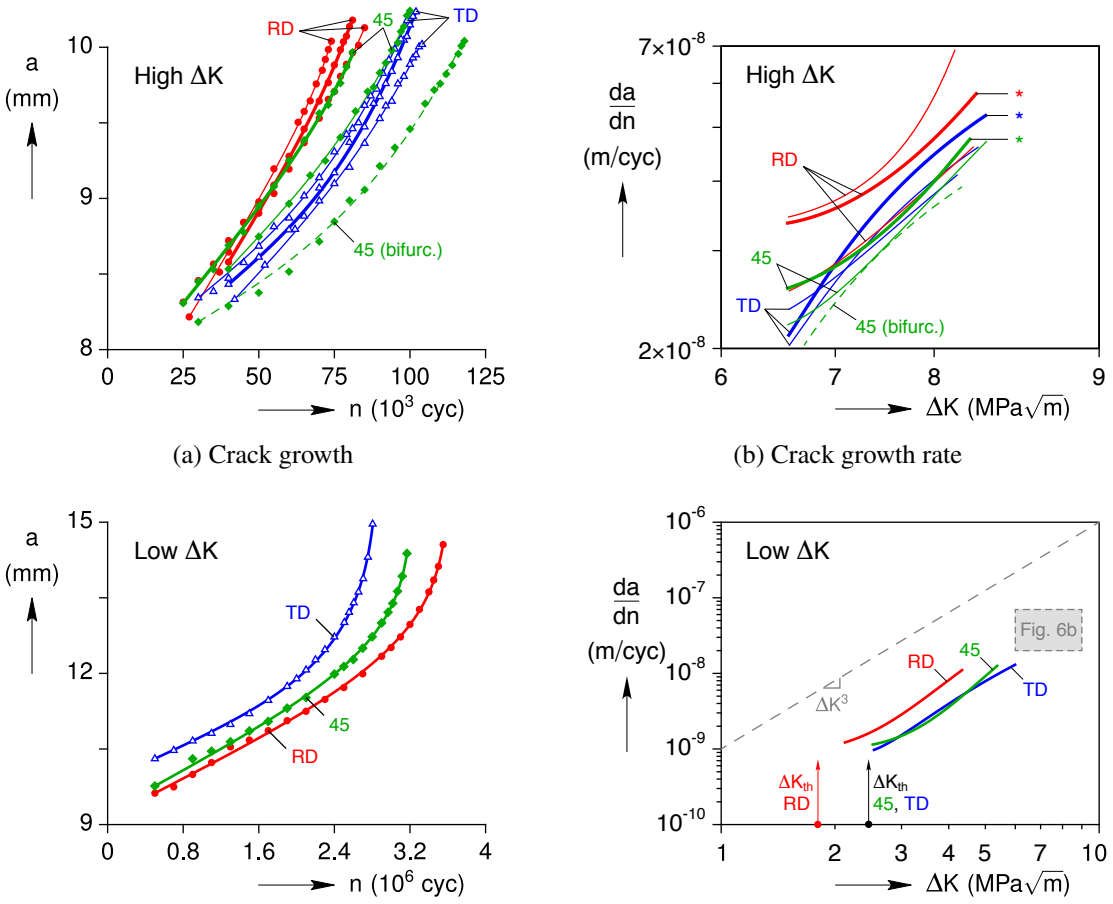

(a) Crack growth

(b) Crack growth rate

(c) Crack growth

(d) Crack growth rate

Figure 7: Fatigue crack growth results: (a) Evolution of crack length (a) with cycle number (n) at high stress intensity amplitude (ΔK) in nine compact tension (CT) samples (3 each for RD, 45, and TD textures). The 45 sample with a bifurcated crack (Figure S10) is indicted. (b) Log-log plot of crack growth rates (da/dn) versus ΔK for the high ΔK experiments. The three samples subjected to microscopic characterization in Section 3.3 are indicated by asterisks. (c) Subsequent evolution of crack length with cycling in three CT samples at low stress intensity amplitude (ΔK). (d) Log-log plot of crack growth rates (da/dn) versus ΔK for the low ΔK experiments. Fatigue thresholds (ΔK_{th}) are shown for each case. The Paris Law ΔK^3 is indicated by the gray dashed line.

3.3. Microscopic Crack Measurements

Crack-tip displacements and strain fields were measured at the microscale for one precracked CT sample of each texture (indicated by asterisks in Figure 7b) during an additional load-unload cycle to K_{max} = 6 MPa $\sqrt{m}$. As measured by SEM-DIC, Figure 8 provides contour plots of the

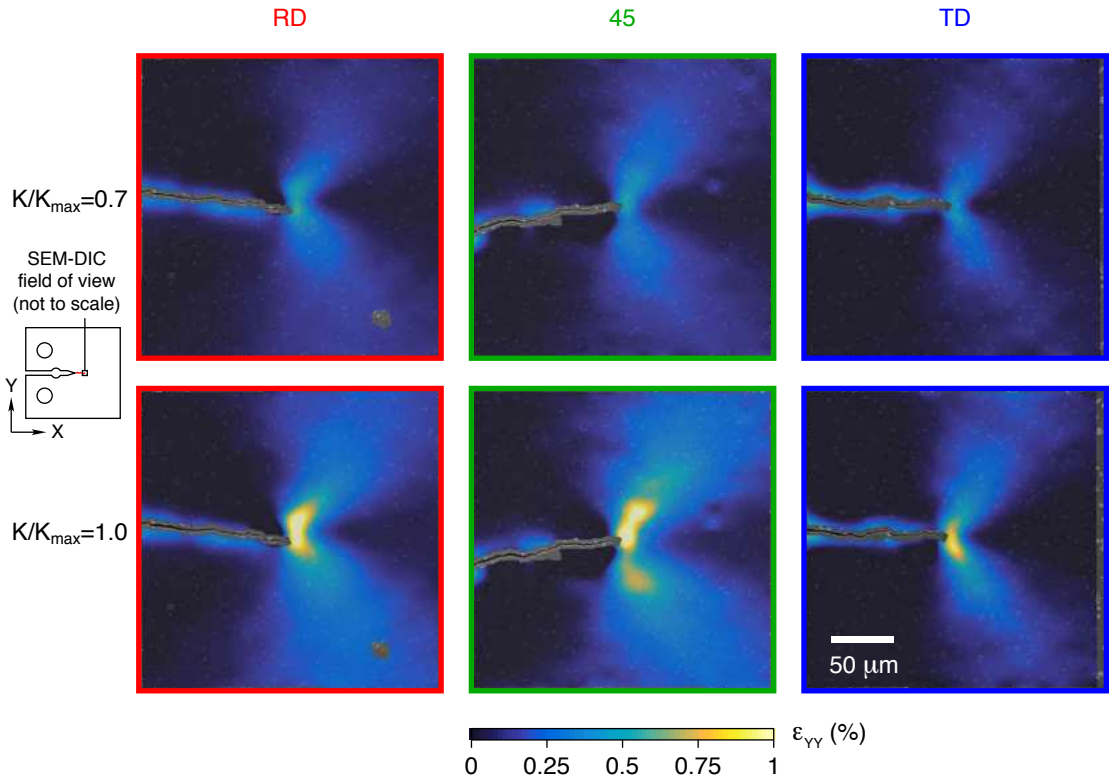

Figure 8: SEM-DIC strain fields (ε_{YY}, perpendicular to the crack direction) for RD, 45, and TD samples at two stress intensities (K_{max} = 6 MPa $\sqrt{m}$). The shape of the high-strain lobes were similar in all three samples, but strain magnitudes were about 1.25× times higher for the RD and 45 than for TD.

strain perpendicular to the crack direction (ε_{YY}) in a 300 μm field of view around the crack tip at two stress intensities, K/K_{max} = 0.7 and 1.0. All three samples exhibited two distinct lobes of strain at $\varepsilon_{YY} > 0.25\%$. At a given stress intensity, lower strains in the vicinity of the crack tip were observed in the TD sample compared to the RD and 45 samples. Gray regions around the crack faces do not have DIC points because the cracks were manually removed from the DIC areas of interest.

SEM-DIC also provided the displacement fields, from which microscopic response curves could be extracted along with displacement profiles very near the crack tip (see Figure 9). Crack-tip coordinates were defined in a local x-y frame with the crack tip at the origin (Figure 9a). Crack separation profiles were defined as the elongation normal to the crack, $\Delta v(x) = v_A(x) + v_B(x)$, between two reference lines symmetrically offset about the crack by h_0 = 20 μm [55]. With subset-based DIC, the data points are inset by half the subset width from the boundary of the AOI. In these SEM-DIC measurements, the AOI did not include the crack, so

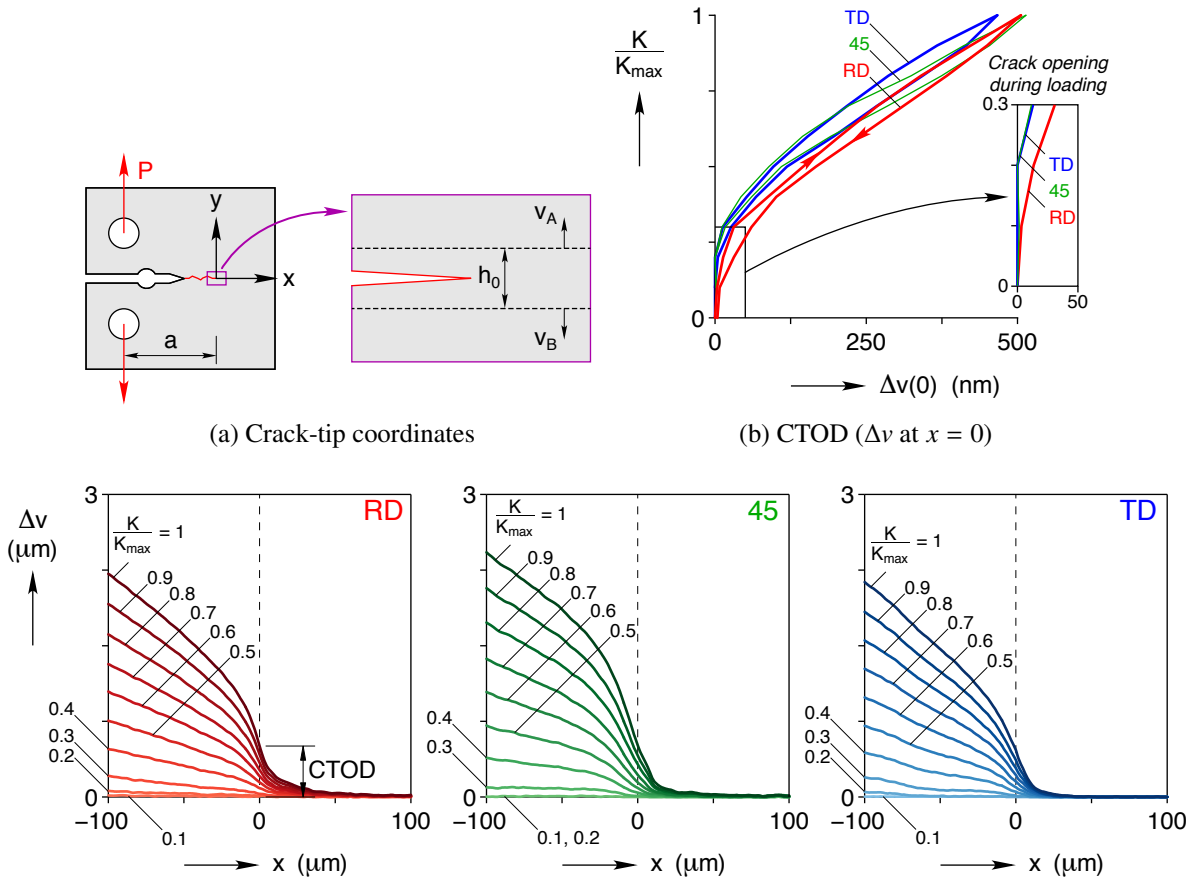

(a) Crack-tip coordinates

(b) CTOD (Δv at $x = 0$)

(c) Crack separation profiles

Figure 9: Microscopic crack opening results from SEM-DIC during a load-unload cycle of three precracked CT samples to $K_{max} = 6$ MPa $\sqrt{m}$: (a) Schematic of local coordinates (x, y) with the crack tip at $(0, 0)$. (b) Microscale load-unload response curves in terms of the crack-tip opening displacement (CTOD) $\Delta v(0)$, where $\Delta v(x) = v_A(x) + v_B(x)$ as shown in (a). (c) Crack separation profiles, $\Delta v(x)$, across the crack tip during loading for each sample.

h_0 was selected as a reasonably small distance between valid DIC points nearest to the crack face.

Microscale load-unload response curves (Figure 9b) were plotted in terms of the normalized stress intensity (K/K_{max}) versus the crack-tip opening displacement (CTOD), defined as CTOD = $\Delta v(0)$. All three samples exhibited a slight hysteresis between loading and unloading, forming a clockwise loop as shown by arrows in the RD case. The RD sample generally had larger crack-tip opening displacements (CTOD) than the 45 and TD samples. As seen in the magnified inset of Figure 9b) during the initial loading, the crack opening was delayed (crack closure) in the 45 and TD responses. The 45 and TD samples remained closed at $K/K_{max} = 0.2$, yet the RD sample

had already opened to about 20 nm. The crack opening threshold (K_{open}) was between 0.6 to 1.2 MPa $\sqrt{m}$ for the RD and between 1.2 and 1.8 MPa $\sqrt{m}$ for the 45 and TD. This is consistent with the RD's lower fatigue threshold and faster crack growth rates seen in Figure 7. Crack closure increases fatigue thresholds, as the crack remains closed during a significant portion of each fatigue cycle [70]. Toughening from crack closure is most prominent at low stress intensities for which the crack unloads to zero effective stress intensity before the applied tensile force reaches zero. This is consistent with the suppressed crack growth rates in the 45 and TD samples at low stress intensities (Figure 7d).

A series of crack separation profiles $\Delta v(x)$ across the crack tip were also plotted for each texture (Figure 9c). The profile shapes were similar between the RD, 45, and TD samples at K_{max}, although the amplitude at the crack mouth ($x = -100\ \mu$m) was interestingly largest for the 45 sample. Other differences were noticed upon close inspection, especially at low K. At $K/K_{max} = 0.2$, crack closure extended behind the crack tip to $x < -100\ \mu$m in the 45 sample, and to about $x = -60\ \mu$m in the TD sample. At $x = -100\ \mu$m, the 45 sample had the smallest Δv at $K/K_{max} = 0.3$, but caught up to the others by Δv at $K/K_{max} = 0.6$ and then surpassed them.

Postmortem fracture surfaces from each sample texture were examined in the SEM at two locations along the fracture surfaces, 1 mm (Figure S11) and 4 mm (Figure S12) from the notch root, but no significant differences were observed among them. At approximately $30,000\times$ magnification, all three sets of fracture surfaces exhibited ductile tearing. Angled ($\approx 45^{o}$) striations from the crack growth direction were evident, possibly due to shear from the relatively thin, nominally plane-stress samples. Transverse striations perpendicular to the crack growth direction, indicating crack-tip blunting and reopening during a fatigue cycle, were found in limited areas of all three samples.

Finally, to summarize all the experimental results of this work, Table I lists key quantitative observations from the material's texture, functional fatigue, and structural fatigue measurements.

Section	Parameter	RD	45	TD
Crystallographic texture (Section 2.1)	⟨1 0 0⟩ (MUD)	0.3	0.3	0.8
	⟨1 1 0⟩ (MUD)	3.7	2.0	1.4
	⟨1 1 1⟩ (MUD)	1.2	0.8	0.4
Stress-limited tension cycles (functional fatigue; Section 3.1)	ε (%) for $n = 1$ at $\sigma = 0.45$ GPa	6.88	6.40	4.91
	σ_p (GPa) for $n = 25$	0.26	0.30	0.35
	σ_p (GPa) for $n \to \infty$	0.24	0.29	0.32
	ε_r (%) for $n = 25$	1.00	0.91	0.41
	ε_r (%) for $n \to \infty$	1.15	0.99	0.48
	W_{net} (MJ/m^3) for $n = 25$	6.89	6.47	4.95
Crack growth (structural fatigue; Section 3.2)	K_{th} (MPa $\sqrt{m}$)	1.8	2.4	2.4
	da/dn (m/cyc) at $\Delta K = 4$ MPa $\sqrt{m}$	8.0×10^{-9}	3.5×10^{-9}	4.0×10^{-9}
	da/dn_{avg} (m/cyc) at $\Delta K = 8$ MPa $\sqrt{m}$	4.7×10^{-8}	3.8×10^{-8}	4.0×10^{-8}
Microscopic crack opening (structural fatigue; Section 3.3)	CTOD (nm) at $K = 6$ MPa $\sqrt{m}$	510	510	470
	K_{open} (MPa $\sqrt{m}$)	0.6 to 1.2	1.2 to 1.8	1.2 to 1.8

Table I: Summary of key observations for crystallographic texture, functional fatigue, and structural fatigue for the three sample textures.

4. Discussion

4.1. Effects of Texture on the Functional Fatigue of NiTi

The effects of texture on functional fatigue in our work are consistent with the underlying micro-mechanisms of slip and martensitic transformation noted in the literature (Table II). The TD sample exhibited the most resistance to functional fatigue compared to the RD and 45 samples. Specifically, tension along the TD resulted in the lowest residual strain accumulation (Figure 3c) and the slowest rate of shakedown of the loading ($A \to M$) plateau stress (Figure 3b). The likely reason for this stems from the texture measurements of Section 2.1, which are worth reviewing. The IPF for TD in Figure 1 had a relatively flat distribution across the stereographic triangle, while the RD and 45 directions had clear peaks at [1 1 0]. Referring to Table I, large amounts of [1 1 0] were measured in the RD (3.7 MUD) and 45 (2.0 MUD) samples and less so in the TD sample (1.4 MUD). Likewise, similar trends held between the samples for [1 1 1], although the respective magnitudes were less by about 1/3×. The TD had a mild density of [1 0 0] (0.8 MUD), yet [1 0 0] was mostly absent in RD and 45 (0.3 MUD). In fact, TD had the highest density of [1 0 0] orientations anywhere in the plane of the sheet (see the perimeter of the pole figures in

Mechanisms of plasticity and transformation	→	**Observations of functional fatigue in present work**
• Highly reversible transformation for deformation along ⟨1 0 0⟩ [16–19], near the theoretical maximum Schmid factor for $\langle 1\,1\,0\rangle_M$ type II twins [18]	→	Lower residual strain accumulation in **TD** (Figure 3), the in-plane sheet direction with the most (1 0 0) orientations (Figure 1)
• Lack of transformation and large irreversible strain after unloading for deformation along ⟨1 1 1⟩ [16–19], which is oriented favorably for slip [16]	→	Higher residual strain accumulation in **RD** (Figure 3), the in-plane sheet direction with the most (1 1 1) orientations (Figure 1)
• Twice as much M in single CV domains during first cycle tension along **RD** than **TD** [41], leading to higher residual strain accumulation and more prevalent martensite strain memory, presumably from more extensive or intensive dislocation networks [12]	→	Higher residual strain accumulation (Figure 3) and macroscopic martensite strain memory (Figure 5) in **RD**

Table II: Mechanisms of plasticity and martensitic transformation from prior work on NiTi SMAs confirmed by observations of functional fatigue in the present work.

Figure S5a).

Based on crystal plasticity arguments, the prevalence of [0 1 1] and [1 1 1] directions in the RD and 45 tension samples suggests they would suffer more slip activity than the TD sample during uniaxial tension. As noted in [16, 18], the dominant slip systems in B2 NiTi are the {0 0 1}⟨1 0 0⟩ and {0 1 1}⟨1 0 0⟩ families, and they computed the Schmid factors for plastic flow during uniaxial loading. They showed that the Schmid factor is zero (in both slip systems) for loading along [1 0 0]. Furthermore, the Schmid factor is maximum for loading along [0 1 1] in the first slip system and loading near [1 1 1] in the second slip system. These suggest that plastic slip is suppressed for [1 0 0] loading, yet is maximally promoted for the other two, [0 1 1] and [1 1 1] loading. Prior works on cold-rolled NiTi measured the dominant textures to be (1 1 0)[1 $\bar{1}$ 0] and (1 1 1)[1 $\bar{1}$ 0] [22, 35, 37]. These works saw minimum strain ratcheting in the TD case, consistent with our results in Figure 3c, and they also attributed it to the near zero Schmid factor of their TD texture for plastic slip.

Other factors may also have played a role in the functional fatigue performance, related to the different microstructures and particular martensite variants that formed during the tensile experiments. For example, microscopic observations during tension along the RD and TD of a superelastic NiTi sheet, much like ours, showed that the RD sample had about twice the volume fraction of martensite as single CV domains (48%) compared to the TD sample (25%) [41]. As the RD sample in the present work likely also exhibited a higher volume fraction of martensite as single CV domains, the increased rate of functional fatigue for the RD case could be related to the large austenite-CV incompatibility [12]. Nevertheless, this also likely leads to irreversible plastic

flow, so we believe that the resistance (or lack of resistance) to plastic slip is the overriding factor, at least for stress-limited cycling.

The repeated occurrence of strain localization at the same point in the sample (45 and RD) seems to suggest that the first localization event created a local residual stress field (likely with irreversible plastic slip and locked-in martensite) that encouraged transformation to first occur at that location during later cycles. This local 'damaged' region was then the last location to revert to austenite upon unloading. The TD sample, apparently, did not suffer the same damage during its first localization event, which led to its higher reversibility (smaller residual strain accumulation). Without any prior-induced stress concentration or locked-in martensite to act as an imperfection to bias where strain localization (macroscopic nucleation) would start, the position of the localization event jumped around from cycle to cycle. Also, this observation is consistent with the few special SMAs with nearly perfect austenite-martensite compatibility and excellent reversibility, that also exhibit changes in the transformation morphology from cycle to cycle [8]. By contrast, NiTi does not have perfect austenite-martensite compatibility, and commercial suppliers usually provide it in the RD (or similar) texture. Thus, usually one observes the same morphologies of martensite reappearing at the same locations at both the macroscale [11] and microscale [12] during successive cycles. Regarding the cyclic behavior of SMAs, it is interesting that *repeatability* of the strain field during transformation and *reversibility* of the deformation (and energy) are at odds with one another.

In terms of design of NiTi devices, there exists a trade-off between functional fatigue performance and magnitude of transformation strain. Tension along the RD provides the largest recoverable strain, consistent with prior experiments and modeling [20]. However, cyclic tension along the TD results in the slowest strain ratcheting. If lower transformation strains and higher transformation stresses are suitable for an application under stress-controlled fatigue, then the device should be fabricated to keep the major principal stress aligned with the texture akin to the TD texture, i.e., with a higher density of [1 0 0] and lower density of [1 1 1] and [1 1 0].

4.2. *Effects of Texture on the Structural Fatigue of NiTi*

Most, but not all, of the trends in texture orientation observed for functional fatigue also hold for structural fatigue. In terms of structural fatigue, the TD samples generally outperformed the RD samples at both the macroscale and microscale. At the macroscale, the TD had slower crack growth during both high ΔK and low ΔK cycling, had a larger fatigue threshold (K_{th}), and exhibited a more jagged crack path. At the microscale, the TD had a smaller strain magnitude in the vicinity of the crack trip and exhibited a higher crack opening threshold (K_{open}) than the TD.

It is not always the case, however, that enhanced functional fatigue correlates with better structural fatigue performance. For example, in the authors' previous work on grain size effects in NiTi fatigue crack growth [55], nanocrystalline NiTi had an impressive resistance to plastic deformation under tensile cycling [71], yet its superior functional fatigue resistance did not translate to superior structural fatigue resistance. Rather, the roughness-induced crack closure in the coarse-grained NiTi provided sufficient crack growth resistance to overcome its relatively poor plasticity resistance [55]. Here, fortunately, we do not need to worry about differences in grain size, and the similarity of the fracture surfaces for RD, 45, and TD (Figures S11 and S12) indicates that the structural fatigue responses were not affected by differences in roughness-induced crack closure.

The differences in fatigue thresholds and crack growth rates (Figure 7) are likely driven by the same anisotropic crystal plasticity considerations discussed above for functional fatigue. As fatigue cracking originates from plastic deformation, the reduced accumulation of plastic strain in the TD likely contributed to an intrinsic toughening mechanism that reduced its crack growth rates compared to the RD. The larger fatigue thresholds of 45 and TD indicate that their textures imparted a toughening mechanism that acted at low stress intensities. Likely, this was a result of intrinsic toughening, as toughening at low stress intensities generally arises from intrinsic toughening mechanisms [72, 73].

Our results are also consistent with related prior work on monotonic fracture in terms of the density of grains oriented favorably for cracking. The lower density of [1 0 0] and higher density of [1 1 1] in the RD corresponds to the directions of poor fracture resistance in single crystals of NiTi [47]. Furthermore, (1 1 0) grains with respect to the tensile axis have been shown to be likely sites for crack initiation and growth [44]. Our RD had the highest density of [1 1 0] for any in-plane direction (Figure S5a).

The optical micrographs in Figure 6 also show a relatively straight crack path in the RD sample but more jagged (meandering) paths in the 45 and TD samples, which suggests an extrinsic toughening mechanism may be present for the 45 and TD cases. Close inspection of the crack paths at the microscale (Figure 8) also indicate jagged crack paths in the 45 and

TD samples. Jagged crack paths (called 'crack deflection' in [72, 73]) may have contributed to their slower crack growth rates, perhaps to the highest degree in the 45 samples. The occurrence of a bifurcated crack (Figure S10) in one of the 45 samples is suggestive, but not conclusive. Crack deflection could be more prevalent in the 45 texture, or the oblique texture may have inherently caused the crack to deflect off-axis. As the 45 and TD samples had the same fatigue threshold and similar crack growth rates (Figure 7d), yet distinct textures, intrinsic toughening from anisotropy is probably not the only toughening mechanism that is different among the RD, 45, and TD samples. Crack deflection, crack bifurcation, and non-straight crack paths have been observed in other fatigue experiments in superelastic NiTi [55, 74, 75]. As there is limited evidence here, future work should examine crack growth rates along more in-plane directions and more samples.

4.3. Similarities and Differences of the 45 Texture with RD and TD

In some measures, fatigue in the 45 texture was similar to the RD, yet in others, it was similar to the TD. A number of factors could be contributing to this. From the texture measurements, RD and 45 had the same density of (1 0 0) orientations, but the 45 had about half the density of (1 1 0) orientations (Figures 1 and S5). In terms of functional fatigue, slightly less residual strain accumulated for tension along the 45 compared to the RD. One explanation for this is the 0.8 MUD of (1 1 1) orientations in the 45, compared to 1.2 MUD of (1 1 1) in the RD. As (1 1 1) has been observed to have poor reversibility [16–19], the lower density of (1 1 1) in the 45 texture could be responsible for its slight improvement in functional fatigue resistance compared to the RD texture.

In terms of structural fatigue, the 45 texture had similar crack growth rates and the same fatigue threshold (2.4 MPa $\sqrt{\text{m}}$) as the TD texture, while the RD texture had the fastest crack growth rates and lowest fatigue threshold (1.8 MPa $\sqrt{\text{m}}$). The density of (1 1 0) orientations in the plane of the sheet was likely important, as (1 1 0) grains with respect to the tensile axis have been identified as probable sites of crack initiation and growth [44]. The densities of the (1 1 0) orientations for the RD, 45, and TD were 3.7, 2.0, and 1.4 MUD, respectively (Figures 1 and S5). Furthermore, although the evidence is limited to a small number of samples, crack deflection could be a secondary factor for increasing the fatigue crack growth resistance of the 45 samples, as discussed in Section 4.2.

5. Conclusions

The functional and structural fatigue of commercially available, slightly Ni-rich (superelastic) cold-rolled NiTi sheet was characterized with respect to crystallographic texture for three in-plane directions: 0° rolling direction (RD), 45° oblique direction (45), and 90° transverse direction (TD).

Texture was measured by X-ray diffraction to generate an orientation distribution function (ODF) and to plot inverse pole figures (IPFs) for the normal direction (ND) to the sheet and the RD, 45, and TD directions. Functional fatigue was measured during superelastic tension experiments with cycling and was evaluated by the accumulation of plastic strain and the reduction of transformation stress plateaus. Structural fatigue was characterized by cyclic experiments on compact tension samples through macroscopic crack growth rates, fatigue crack thresholds, and microscale crack-tip displacements and strain fields. All test samples were cut from the same sheet of NiTi to avoid introducing unwanted variations in alloy composition, grain size, and precipitates.

Key observations and conclusions of this work are:

- The local maxima in the orientation distribution indicated a biaxial texture in the NiTi sheet of $(1\,1\,1)[1\,\bar{1}\,0]$. In the plane of the sheet, the IPFs indicated local maxima at [1 1 0] for all three directions studied, but the peaks trended from strong to mild for RD, to 45, to TD. Similar trends, but of lesser magnitude, were measured for the [1 1 0] direction. The [1 0 0] direction was largely absent in the RD and 45 cases but mildly present in the TD case. The relatively high density of [1 1 0] and [1 1 1] directions in the RD and 45 samples (compared to the TD sample) seemed to have adverse repercussions on their functional fatigue and structural fatigue performance. Likely, this was due to the near maximal Schmid factors for slip when loaded along [1 1 0] and [1 1 1] and the zero Schmid factor for loading along [1 0 0].

- After 25 load-unload cycles in uniaxial tension, the TD sample accumulated half the residual strain than in the RD sample. This appears to be due to the higher resistance to plastic slip in the TD sample as a result of the sheet texture.

- While the phase transformation consistently localized macroscopically in the same places in the gauge sections of the RD and 45 samples, macroscopic localization in the TD sample varied oddly from cycle to cycle. Interestingly, certain rare SMAs with nearly perfect austenite-martensite compatibility and reversibility also transform in this way, with very different martensite structures forming from cycle to cycle [8]. Both the TD sample and the rare SMA from [8] seem to avoid plastic flow, one by its high resistance to slip and the other by eliminating the need for slip. These seems to avoid the history-dependence on where martensite should form upon subsequent cycles, as is the usually observed case when plastic flow cannot be avoided during martensitic transformation.

- The fatigue crack thresholds were larger for 45 and TD (2.4 MPa $\sqrt{\text{m}}$) than for RD (1.8 MPa $\sqrt{\text{m}}$) at the stress ratio $R = 0.1$. Since crack closure effects can increase the fatigue threshold, this macroscopic finding correlated well with microscopic observations of crack

closure. The RD crack tip opened at about 0.9 MPa $\sqrt{m}$, while the 45 and TD crack tips opened at about 1.5 MPa $\sqrt{m}$.

- For fatigue cracking at high stress intensity amplitudes ΔK, the crack growth rate of the RD samples was about 1.25× that of the TD samples. At low ΔK, the crack growth rate of the RD sample was twice that of the 45 and TD samples. The 45 and TD samples also had more jagged (meandering) crack paths than the RD samples. No significant differences were observed in the fracture surfaces, so differences arising from roughness-induced crack closure were ruled out. Rather, we suspect that the lack of resistance to plastic slip in the RD sample intrinsically led to increased plastic flow, which promoted fatigue crack growth.

For current and future NiTi applications, this work suggests a potential texture-optimized design approach to mitigate fatigue. If other micro-structural factors (e.g. composition, grain size, and precipitates) are similar to those studied here and if the design constraints can accommodate lower transformation strains and higher transformation stresses, then the maximum tensile stresses in the device should align with the texture akin to the TD texture, i.e., with a higher density of [1 0 0] and lower density of [1 1 1] and [1 1 0]. Along this direction, both the functional fatigue (accumulation of residual strain and reduction in plateau stress) and structural fatigue (crack growth rate) will be minimized under stress-controlled cycling. Of course, this approach has only been assessed here with respect to uniaxial tension and plane stress with a dominant maximum principal stress (notched CT specimen), and may not work for more general (strongly multiaxial) stress states. This could, however, motivate future research to assess the influence of other stress states on the texture-dependent fatigue performance of NiTi-based SMAs.

Acknowledgments

We are thankful to Harshad Paranjape, Alan Pelton, and Michael Thouless for insightful discussions; to Nakhiah Goulbourne for generously sharing fatigue testing equipment; to Zhe Chen, Mark Cornish, William Lenthe, and Darin Randall for assistance with SEM-DIC experiments; to J.C. Stinville for assistance with TSEM experiments; to Jerry Zhongrui Li and Ying Qi for assistance with X-ray diffraction measurements; to Anthony Rollett for guidance on texture and anisotropy and for permission to adapt Figure S3 from his course notes; to Ralf Hielscher for support with MTEX; to Keigo Nagao for details about Rigaku in-plane pole figure measurements; and to the University of Michigan Materials Science and Engineering Department, the University of Michigan Robert B. Mitchell Electron Microbeam Analysis Lab, and the Michigan Center for Materials Characterization for instrument use and staff assistance.

Funding

This work was supported by the National Science Foundation (CAREER Award, CMMI 1251891) and the Department of Defense (National Defense Science and Engineering Graduate Fellowship program, 32 CFR 168a).

References

[1] Duerig T, Pelton A, Sto D (1999) An overview of nitinol medical applications. Materials Science & Engineering A 275:149–160, doi:10.1016/S0921-5093(99)00294-4

[2] NASA (2018), Reinventing the Wheel. https://www.nasa.gov/specials/wheels/

[3] Pelton A (2011) Nitinol fatigue: a review of microstructures and mechanisms. Journal of Materials Engineering and Performance 20(4-5):613–617, doi:10.1007/s11665-011-9864-9

[4] Eggeler G, Hornbogen E, Yawny A, Heckmann A, Wagner M (2004) Structural and functional fatigue of NiTi shape memory alloys. Materials Science and Engineering A 378(1-2 SPEC. ISS.):24–33, doi:10.1016/j.msea.2003.10.327

[5] Furgiuele F, Magarò P, Maletta E Carmine andSgambitterra (2020) Functional and Structural Fatigue of Pseudoelastic NiTi: Global Vs Local Thermo-Mechanical Response. Shap. Mem. Superelasticity. Shape Memory and Superelasticity doi:10.1007/s40830-020-00289-9

[6] Bowers M, Gao Y, Yang L, Gaydosh D, De Graef M, Noebe R, Wang Y, Mills M (2015) Austenite grain refinement during load-biased thermal cycling of a Ni49.9Ti50.1 shape memory alloy. Acta Materialia 91:318–329, doi:10.1016/j.actamat.2015.03.017

[7] Gao Y, Casalena L, Bowers M, Noebe R, Mills M, Wang Y (2017) An origin of functional fatigue of shape memory alloys. Acta Materialia 126:389–400, doi:10.1016/j.actamat.2017.01.001

[8] Song Y, Chen X, Dabade V, Shield TW, James RD (2013) Enhanced reversibility and unusual microstructure of a phase-transforming material. Nature 502(7469):85, doi:10.1038/nature12532

[9] Norfleet D, Sarosi P, Manchiraju S, Wagner MX, Uchic M, Anderson P, Mills M (2009) Transformation-induced plasticity during pseudoelastic deformation in Ni–Ti microcrystals. Acta Materialia 57(12):3549–3561, doi:10.1016/j.actamat.2009.04.009

[10] Bowers M, Chen X, De Graef M, Anderson PM, Mills M (2014) Characterization and modeling of defects generated in pseudoelastically deformed NiTi microcrystals. Scripta Materialia 78:69–72, doi:10.1016/j.scriptamat.2014.02.001

[11] Kim K, Daly S (2010) Martensite Strain Memory in the Shape Memory Alloy Nickel-Titanium Under Mechanical Cycling. Experimental Mechanics 51(4):641–652, doi:10.1007/s11340-010-9435-2

[12] Kimiecik M, Jones JW, Daly S (2016) The effect of microstructure on stress-induced martensitic transformation under cyclic loading in the SMA Nickel-Titanium. Journal of the Mechanics and Physics of Solids 89:16–30, doi:10.1016/j.jmps.2016.01.007

[13] Miyazaki S, Kimura S, Otsuka K, Suzuki Y (1984) The habit plane and transformation strains associated with the martensitic transformation in Ti-Ni single crystals. Scripta metallurgica 18(9):883–888, doi:10.1016/0036-9748(84)90254-0

[14] Sehitoglu H, Wu Y, Alkan S, Ertekin E (2017) Plastic deformation of B2-NiTi–is it slip or twinning? Philosophical Magazine Letters 97(6):217–228, doi:10.1080/09500839.2017.1316019

[15] Gall K, Sehitoglu H, Chumlyakov YI, Zuev YL, Karaman I (1998) The role of coherent precipitates in martensitic transformations in single crystal and polycrystalline Ti-50.8at%Ni. Scripta Materialia 39(6):699–705, doi:10.1016/S1359-6462(98)00236-X

[16] Sehitoglu H, Karaman I, Anderson R, Zhang X, Gall K, Maier H, Chumlyakov Y (2000) Compressive response of NiTi single crystals. Acta Materialia 48(13):3311–3326, doi:10.1016/S1359-6454(00)00153-1

[17] Gall K, Maier H (2002) Cyclic deformation mechanisms in precipitated NiTi shape memory alloys. Acta Materialia 50(18):4643–4657, doi:10.1016/S1359-6454(02)00315-4

[18] Gall K, Dunn ML, Liu Y, Labossiere P, Sehitoglu H, Chumlyakov YI (2002) Micro and macro deformation of single crystal NiTi. Journal of Engineering Materials and Technology 124(2):238–245, doi:10.1115/1.1416684

[19] Pfetzing-Micklich J, Ghisleni R, Simon T, Somsen C, Michler J, Eggeler G (2012) Orientation dependence of stress-induced phase transformation and dislocation plasticity in NiTi shape memory alloys on the micro scale. Materials Science and Engineering: A 538:265–271, doi:10.1016/j.msea.2012.01.042

[20] Shu Y, Bhattacharya K (1998) The influence of texture on the shape-memory effect in polycrystals. Acta Materialia 46(15):5457–5473, doi:10.1016/S1359-6454(98)00184-0

[21] Bhattacharya K, Kohn RV (1996) Symmetry, texture and the recoverable strain of shape-memory polycrystals. Acta Materialia 44(2):529–542, doi:10.1016/1359-6454(95)00198-0

[22] Mulder JH, Thoma PE, Beyer J (1993) Anisotropy of the shape memory effect in tension of cold-rolled 50.8 Ti 49.2 Ni (at.%) sheet. Zeitschrift fuer Metallkunde/Materials Research and Advanced Techniques 84(7):501–508

[23] Robertson SW, Imbeni V, Wenk HR, Ritchie RO (2005) Crystallographic texture for tube and plate of the superelastic/shape-memory alloy Nitinol used for endovascular stents. Journal of biomedical materials research Part A 72(2):190–9, doi:10.1002/jbm.a.30214

[24] Robertson SW, Imbeni V, Wenk HR, Ritchie RO (2006) Erratum: Crystallographic texture for tube and plate of the superelastic/shape-memory alloy nitinol used for endovascular stents. Journal of Biomedical Materials Research Part A 78A(2):432–432, doi:10.1002/jbm.a.30841

[25] Robertson SW, Gong XY, Ritchie RO (2006) Effect of product form and heat treatment on the crystallographic texture of austenitic Nitinol. Journal of Materials Science 41(3):621–630, doi:10.1007/s10853-006-6478-y

[26] Luo J, Bobanga JO, Lewandowski JJ (2017) Microstructural heterogeneity and texture of as-received, vacuum arc-cast, extruded, and re-extruded NiTi shape memory alloy. Journal of Alloys and Compounds 712:494–509, doi:10.1016/j.jallcom.2017.04.152

[27] Gall K, Yang N, Sehitoglu H, Chumlyakov YI (2001) Fracture of precipitated NiTi shape memory alloys. International Journal of Fracture 109(2):189–207, doi:10.1023/A:1011069204123

[28] Šittner P, Lukáš P, Novák V, Daymond M, Swallowe G (2004) In situ neutron diffraction studies of martensitic transformations in NiTi polycrystals under tension and compression stress. Materials Science and Engineering: A 378(1-2):97–104, doi:10.1016/j.msea.2003.09.112

[29] Mao S, Luo J, Zhang Z, Wu M, Liu Y, Han X (2010) EBSD studies of the stress-induced B2-B19' martensitic transformation in NiTi tubes under uniaxial tension and compression. Acta Materialia 58(9):3357–3366, doi:10.1016/j.actamat.2010.02.009

[30] Monasevich L, Paskal YI, Prib V, Timonin G, Chernov D (1979) Effect of texture on the shape memory effect in titanium nickelide. Metal Science and Heat Treatment 21(9):735–737, doi:10.1007/BF00708647

[31] Li D, Wu X, Ko T (1990) The texture of Ti-51.5 at.% Ni rolling plate and its effect on the all-around shape memory effect. Acta Metallurgica et Materialia 38(1):19–24, doi:10.1016/0956-7151(90)90130-9

[32] Inoue H, Miwa N, Inakazu N (1996) Texture and shape memory strain in TiNi alloy sheets. Acta Materialia 44(12):4825–4834, doi:10.1016/S1359-6454(96)00120-6

[33] Liu Y, Xie Z, Van Humbeeck J, Delaey L (1999) Effect of texture orientation on the martensite deformation of NiTi shape memory alloy sheet. Acta Materialia 47(2):645–660, doi:10.1016/S1359-6454(98)00376-0

[34] Hornbogen E, Brückner G, Gottstein G (2002) Microstructure and Texture of Ausformed NiTi: In Memoriam Prof. Dr. rer. nat. Dr. hc Kurt Lücke (* June 28, 1921,† October 7, 2001). Zeitschrift für Metallkunde 93(1):3–6, doi:10.3139/146.020003

[35] Chang S, Wu S (2004) Textures in cold-rolled and annealed Ti50Ni50 shape memory alloy. Scripta materialia 50(7):937–941, doi:10.1016/j.scriptamat.2004.01.009

[36] Laplanche G, Kazuch A, Eggeler G (2015) Processing of NiTi shape memory sheets - Microstructural heterogeneity and evolution of texture. Journal of Alloys and Compounds 651:333–339, doi:10.1016/j.jallcom.2015.08.127

[37] Shuai J, Xiao Y (2020) In-Situ Study on Texture-Dependent Martensitic Transformation and Cyclic Irreversibility of Superelastic NiTi Shape Memory Alloy. Metallurgical and Materials Transactions A 51(2):562–567, doi:10.1007/s11661-019-05563-9

[38] Bhattacharya K (2003) Microstructure of martensite: why it forms and how it gives rise to the shape-memory effect, vol. 2. Oxford University Press

[39] Paranjape H, Anderson PM (2014) Texture and grain neighborhood effects on Ni–Ti shape memory alloy performance. Modelling and Simulation in Materials Science and Engineering 22(7):075002, doi:10.1088/0965-0393/22/7/075002

[40] Paul PP, Paranjape HM, Tamura N, Chumlyakov YI, Brinson LC (2020) In-situ, microscale characterization of heterogeneous deformation around notch in martensitic Shape Memory Alloy. Materials Science and Engineering: A 771:138605, doi:10.1016/j.msea.2019.138605

[41] Kimiecik MG (2015) Quantitative Studies of Microstructural Phase Transformation: Critical Features of Nickel Titanium Polycrystals Undergoing Superelastic Deformation. Ph.D. thesis, University of Michigan

[42] Laplanche G, Birk T, Schneider S, Frenzel J, Eggeler G (2017) Effect of temperature and texture on the reorientation of martensite variants in NiTi shape memory alloys. Acta Materialia 127:143–152, doi:10.1016/j.actamat.2017.01.023

[43] Robertson S, Mehta A, Pelton AR, Ritchie R (2007) Evolution of crack-tip transformation zones in superelastic Nitinol subjected to in situ fatigue: A fracture mechanics and synchrotron X-ray microdiffraction analysis. Acta Materialia 55(18):6198–6207, doi:10.1016/j.actamat.2007.07.028

[44] Paul PP, Fortman M, Paranjape HM, Anderson PM, Stebner AP, Brinson LC (2018) Influence of Structure and Microstructure on Deformation Localization and Crack Growth in NiTi Shape Memory Alloys. Shape Memory and Superelasticity 1–9, doi:10.1007/s40830-018-0172-1

[45] Daymond M, Young ML, Almer JD, Dunand DC (2007) Strain and texture evolution during mechanical loading of a crack tip in martensitic shape-memory NiTi. Acta Materialia 55(11):3929–3942, doi:10.1016/j.actamat.2007.03.013

[46] Amin-Ahmadi B, Noebe RD, Stebner AP (2019) Crack propagation mechanisms of an aged nickel-titanium-hafnium shape memory alloy. Scripta Materialia 159:85–88, doi:10.1016/j.scriptamat.2018.09.019

[47] Creuziger A, Bartol L, Gall K, Crone W (2008) Fracture in single crystal NiTi. Journal of the Mechanics and Physics of Solids 56(9):2896–2905, doi:10.1016/j.jmps.2008.04.002

[48] Bachmann F, Hielscher R, Schaeben H (2010) Texture analysis with MTEX - free and open source software toolbox. In Solid State Phenomena, vol. 160, 63–68, Trans Tech Publ, doi:10.4028/www.scientific.net/SSP.160.63

[49] Raabe D, Lücke K (1994) Rolling and annealing textures of BCC metals. In Materials Science Forum, vol. 157, 597–610, Trans Tech Publ, doi:10.4028/www.scientific.net/MSF.157-162.597

[50] Ahadi A, Matsushita Y, Sawaguchi T, Schaffer J, Sun QP, Tsuchiya K (2017) Origin of zero and negative thermal expansion in severely-deformed NiTi alloy. Acta Materialia 124:79–92, doi:10.1016/j.actamat.2016.10.054

[51] LePage W, Daly S, Shaw J (2016) Cross Polarization for Improved Digital Image Correlation. Experimental Mechanics 56:1–27, doi:10.1007/s11340-016-0129-2

[52] Jones E, Reu P (2018) Distortion of digital image correlation (DIC) displacements and strains from heat waves. Experimental Mechanics 58(7):1133–1156, doi:10.1007/s11340-017-0354-3

[53] LePage W, Shaw J, Daly S (2017) Optimum Paint Sequence for Speckle Patterns in Digital Image Correlation. Experimental Techniques doi:10.1007/s40799-017-0192-3

[54] ASTM Standard E561 (2016) E561 standard test method for KR curve determination. ASTM International 1–16

[55] LePage W, Ahadi A, Lenthe W, Sun QP, Pollock T, Shaw J, Daly S (2017) Grain size effects on NiTi shape memory alloy fatigue crack growth. Journal of Materials Research 1–17, doi:10.1557/jmr.2017.395

[56] Wu Y, Ojha A, Patriarca L, Sehitoglu H (2015) Fatigue Crack Growth Fundamentals in Shape Memory Alloys. Shape Memory and Superelasticity doi:10.1007/s40830-015-0005-4

[57] Wu Y, Yaacoub J, Brenne F, Abuzaid W, Canadinc D, Sehitoglu H (2019) Deshielding Effects on Fatigue Crack Growth in Shape Memory Alloys-A study on CuZnAl single-crystalline materials. Acta Materialia doi:10.1016/j.actamat.2019.06.042

[58] Sgambitterra E, Maletta C, Furgiuele F, Sehitoglu H (2018) Fatigue crack propagation in [0 1 2] NiTi single crystal alloy. International Journal of Fatigue 112:9–20, doi:10.1016/j.ijfatigue.2018.03.005

[59] Yaacoub J, Wu Y, Abuzaid W, Canadinc D, Sehitoglu H (2019) Martensite variant localization effects on fatigue crack growth-The CuZnAl example. Scripta Materialia 171:112–117, doi:10.1016/j.scriptamat.2019.06.032

[60] Wang L, Li K, Sanusei S, Ghorbani R, Matta F, Sutton M (2014) Advancement of optical methods in experimental mechanics. In Conference Proceedings of the Society for Experimental Mechanics Series, vol. 3, 289–297, Conference Proceedings of the Society for Experimental Mechanics Series

[61] Cady C, Liu C, Rae P, Lovato M (2009) Thermal and loading dynamics of energetic materials. In Proceedings of the Society of Experimental Mechanics Annual Conference

[62] Liu C, Cady CM, Rae PJ, Lovato ML (2010) On the quantitative measurement of fracture toughness in high explosive and mock materials. Tech. rep., Los Alamos National Lab.(LANL), Los Alamos, NM (United States)

[63] Sutton MA, Li N, Joy D, Reynolds AP, Li X (2007) Scanning electron microscopy for quantitative small and large deformation measurements part I: SEM imaging at magnifications from 200 to 10,000. Experimental mechanics 47(6):775–787

[64] Sutton MA, Li N, Garcia D, Cornille N, Orteu JJ, McNeill S, Schreier H, Li X, Reynolds AP (2007) Scanning electron microscopy for quantitative small and large deformation measurements part II: experimental validation for magnifications from 200 to 10,000. Experimental Mechanics 47(6):789–804

[65] Kammers A, Daly S (2013) Self-Assembled Nanoparticle Surface Patterning for Improved Digital Image Correlation in a Scanning Electron Microscope. Experimental Mechanics 53(8):1333–1341, doi:10.1007/s11340-013-9734-5

[66] Frens G (1973) Controlled Nucleation for the Regulation of the Particle Size in Monodisperse Gold Suspensions. Nature Physical Science 241(105):20–22, doi:10.1038/physci241020a0

[67] Lenthe WC, Stinville JC, Echlin MP, Chen Z, Daly S, Pollock TM (2018) Advanced detector signal acquisition and electron beam scanning for high resolution SEM imaging. Ultramicroscopy 195:93–100, doi:10.1016/j.ultramic.2018.08.025

[68] Barney M, Xu D, Robertson S, Schroeder V, Ritchie R, Pelton A, Mehta A (2011) Impact of thermomechanical texture on the superelastic response of Nitinol implants. Journal of the Mechanical Behavior of Biomedical Materials 4(7):1431–1439, doi:10.1016/j.jmbbm.2011.05.013

[69] Robertson SW, Pelton AR, Ritchie RO (2012) Mechanical fatigue and fracture of Nitinol. International Materials Reviews 57(1):1–37, doi:10.1179/1743280411Y.0000000009

[70] Elber W (1970) Fatigue crack closure under cyclic tension. Engineering Fracture Mechanics 2:37–45, doi:10.1016/0013-7944(70)90028-7

[71] Ahadi A, Sun Q (2014) Effects of grain size on the rate-dependent thermomechanical responses of nanostructured superelastic NiTi. Acta materialia 76:186–197, doi:10.1016/j.actamat.2014.05.007

[72] Ritchie R (1988) Mechanisms of fatigue crack propagation in metals, ceramics and composites: role of crack tip shielding. Materials Science and Engineering: A 103(1):15–28, doi:10.1016/0025-5416(88)90547-2

[73] Ritchie RO (1999) Mechanisms of fatigue-crack propagation in ductile and brittle solids. International Journal of Fracture 100(1):55–83, doi:10.1023/A:1018655917051

[74] Robertson SW, Ritchie RO (2007) In vitro fatigue-crack growth and fracture toughness behavior of thin-walled superelastic Nitinol tube for endovascular stents: A basis for defining the effect of crack-like defects. Biomaterials 28:700–9, doi:10.1016/j.biomaterials.2006.09.034

[75] Chen J, Yin H, Kang G, Sun Q (2018) Fatigue Crack growth in Cold-Rolled and Annealed Polycrystalline Superelastic NiTi Alloys. Acta Mechanica Solida Sinica 1–9, doi:10.1007/s10338-018-0056-0

Supplementary Material

Effects of Texture on the Functional and Structural Fatigue of a NiTi Shape Memory Alloy

William S. LePage[a], John A. Shaw[b], Samantha H. Daly[c,*]

[a]Department of Mechanical Engineering, University of Michigan, 2350 Hayward St., Ann Arbor, MI 48109, USA

[b]Department of Aerospace Engineering, University of Michigan, 1320 Beal Ave., Ann Arbor, MI 48109, USA

[c]Department of Mechanical Engineering, University of California, Santa Barbara, 2355 Engineering II, Santa Barbara, CA 93106, USA

[*]Corresponding author (samdaly@engineering.ucsb.edu).

S1. Differential Scanning Calorimetry

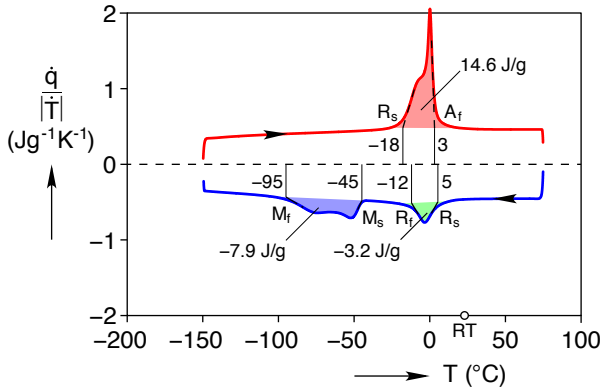

Figure S1: Differential scanning calorimetry (DSC) of the NiTi material indicated an austenite finish temperature of 3 °C. The DSC run used the following sequence: equilibrate at 75 °C; isothermal hold for 1 minute; ramp at 10 °C/min to -150 °C; isothermal hold for 1 minute; ramp at 10 °C/min to 75 °C; and isothermal hold for 1 minute. The experimental method used helium purge gas and calculated the heat capacities directly after calibration with sapphire.

S2. Transmission Scanning Electron Microscopy (TSEM) Imaging

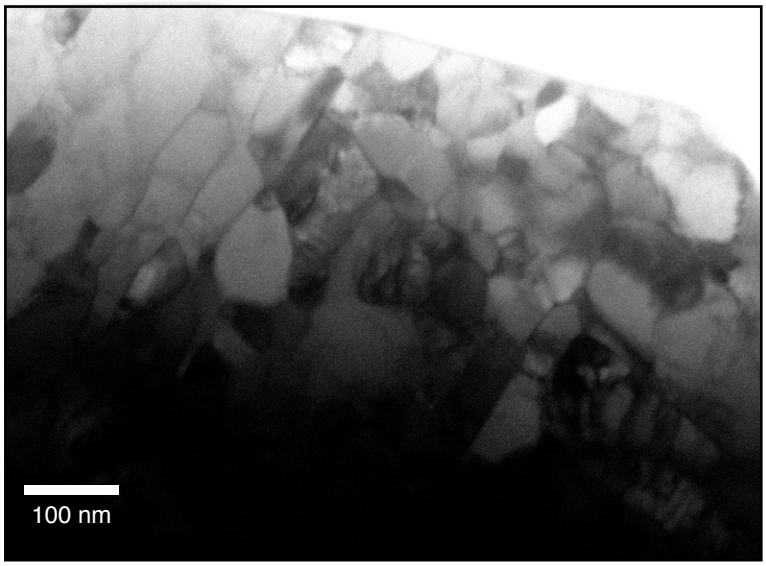

Figure S2: Transmission scanning electron microscopy (TSEM) showed a nanograined structure with grain sizes on the order of 20 to 200 nm. The TSEM foil sample was prepared with the surface normal in the rolling direction of the bulk sheet material. Images were captured with a Thermo Fisher (formerly FEI) Teneo at 30 kV.

S3. Euler Angle Convention

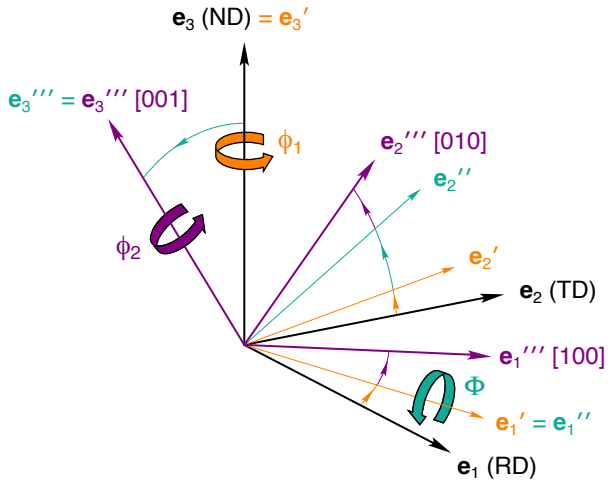

Figure S3: A diagram of the "ZXZ" Bunge Euler angle convention used for the orientation distribution function, adapted from a diagram in lecture notes by Prof. Anthony Rollett, with permission. Starting in the sheet frame with orthornormal base vectors $\{\boldsymbol{e}_1, \boldsymbol{e}_2, \boldsymbol{e}_3\}$ aligned with the respective rolling direction (RD), transverse direction (TD), normal direction (ND), the convention has three successive rotations: ϕ_1 about $\boldsymbol{e}_3$; then Φ about $\boldsymbol{e}_1'$; then ϕ_2 about e_3''. The resulting base vectors $\left\{\boldsymbol{e}_1''', \boldsymbol{e}_2''', \boldsymbol{e}_3'''\right\}$ align with the respective cubic crystal directions [1 0 0], [0 1 0], and [0 0 1].

S4. Pole Figure Measurement, Orientation Distribution Fitting, and Error

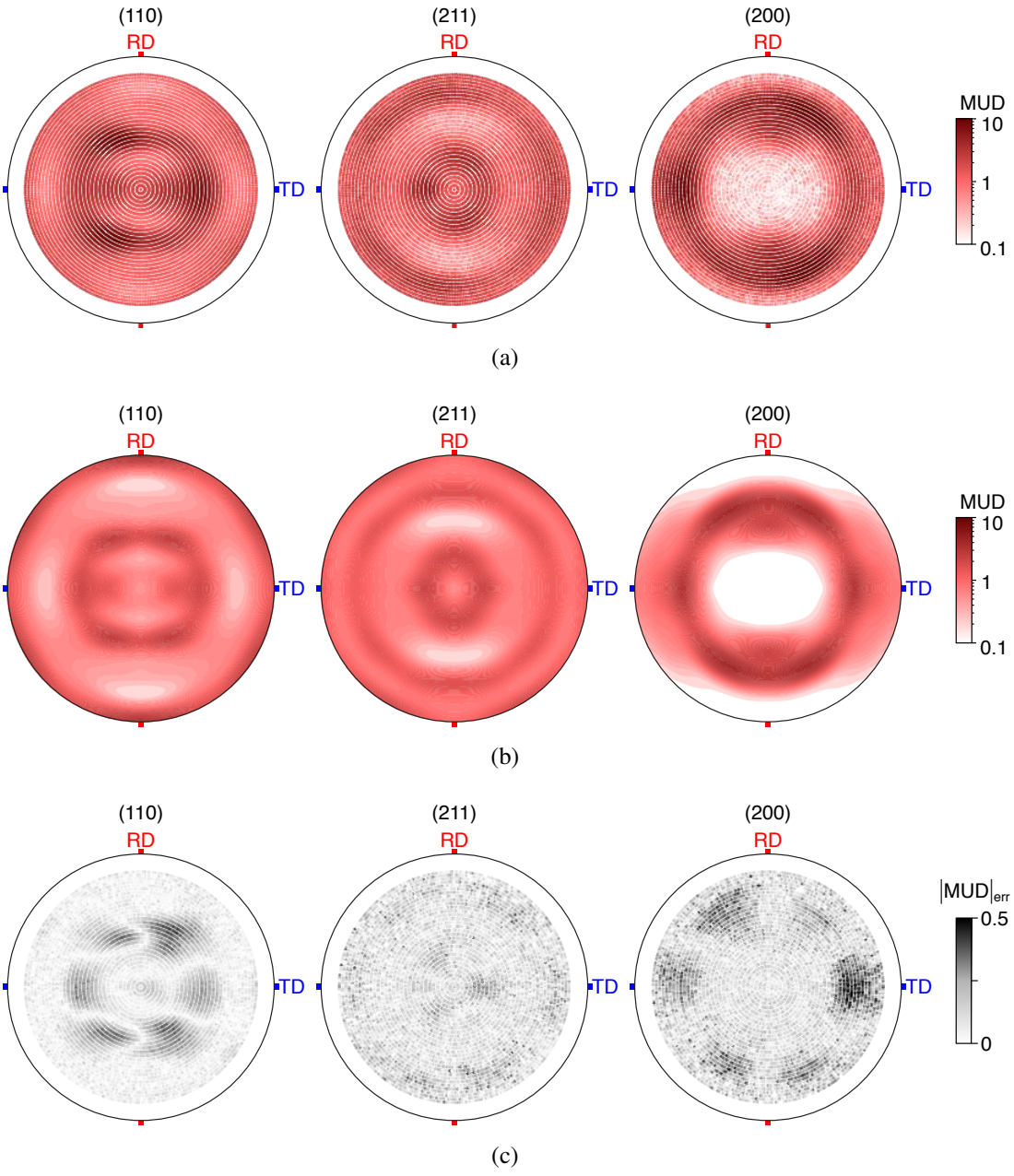

Figure S4: (a) Measured pole figures. (b) Fitted orientation distribution function (ODF). (c) The error in ODF was calculated as the absolute value of the difference between the pole figure measurements and the fitted ODF.

S5. Pole Figures and Inverse Pole figures with (111), (100), and (110) Poles

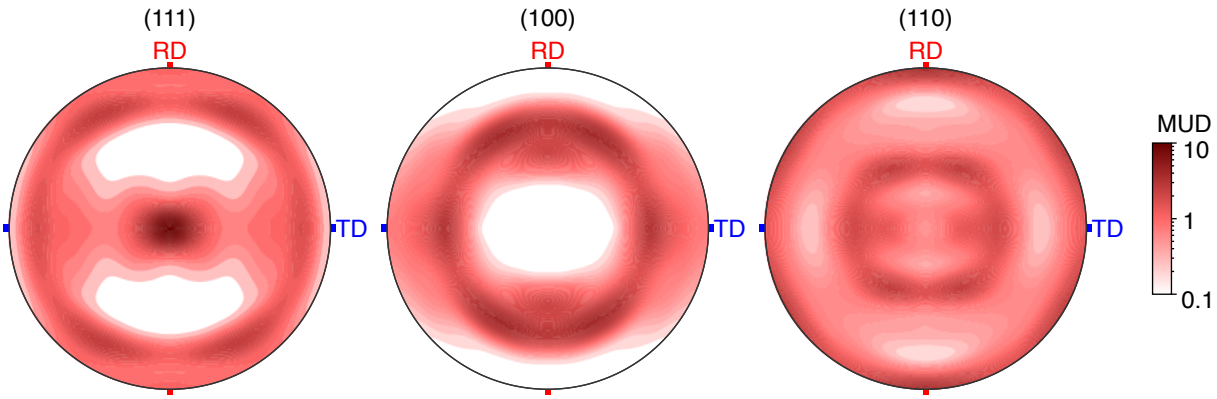

(a)

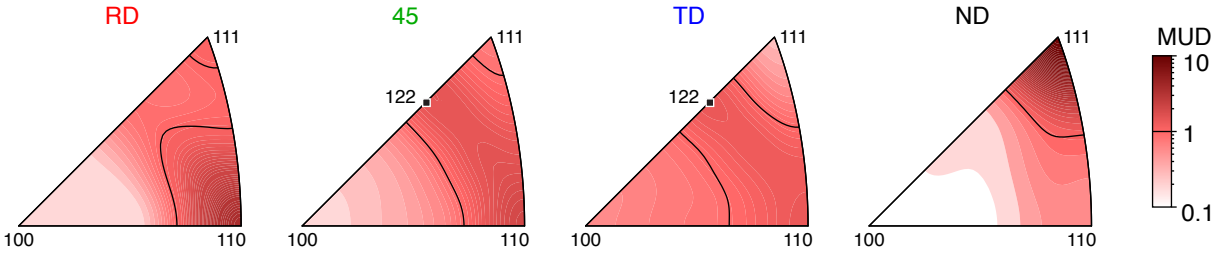

(b)

Figure S5: (a) The orientation distribution function (ODF) of the NiTi sheet at the (1 1 1), (1 0 0), and (1 1 0) poles. (b) Inverse pole figures for the NiTi sheet's rolling direction (RD), 45° from the rolling direction (45), transverse direction (TD), and normal direction (ND). The strongest texture was (1 1 1) in ND (9.4 MUD), and the second strongest texture was (1 1 0) in RD (MUD of 3.7). The maxima for 45 and TD were at (1 1 0), with 2.0 and 1.4 MUD, respectively.

S6. Orientation Distribution Function with respect to Bunge Euler Angles

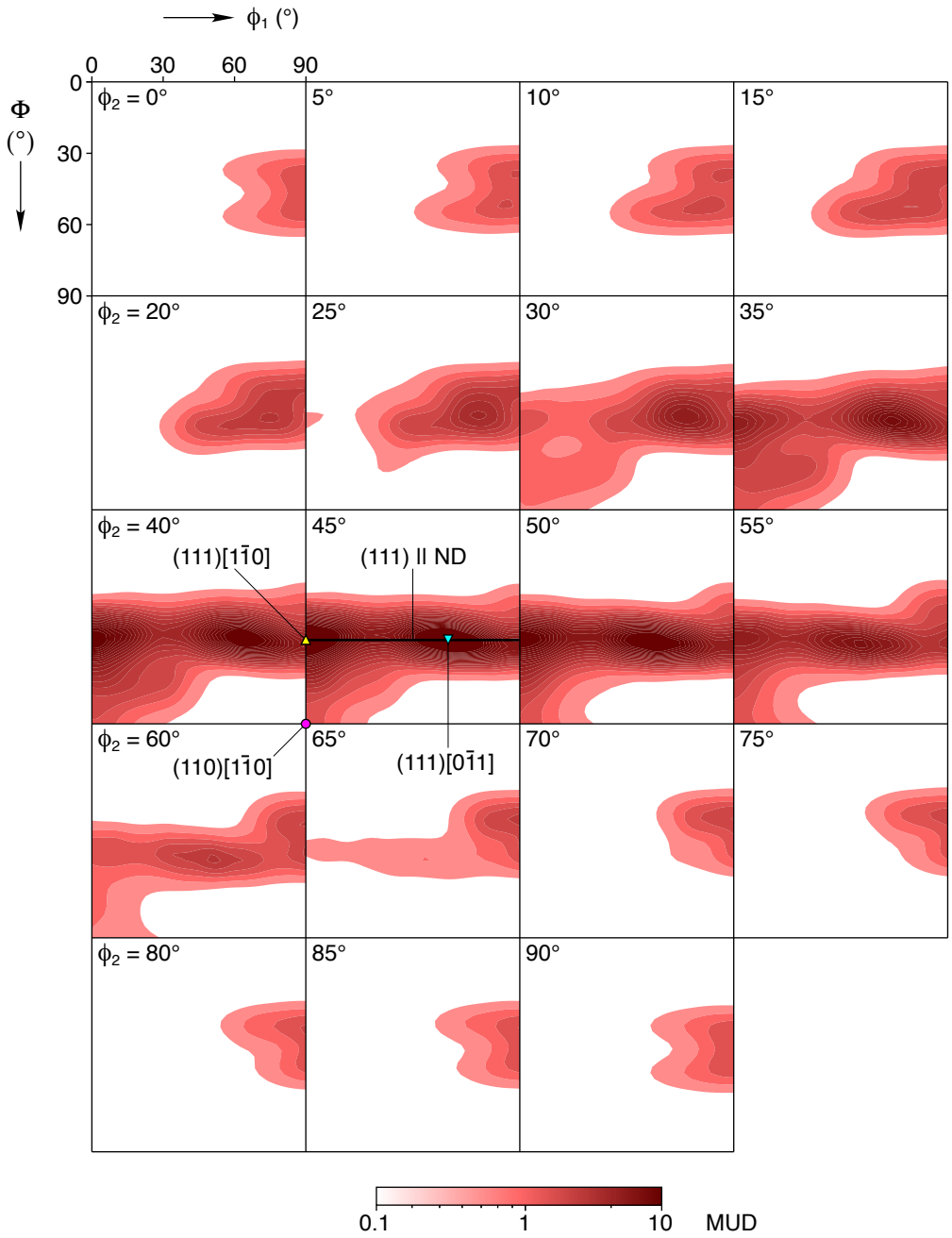

Figure S6: A strong γ-fiber texture, (1 1 1)||ND, was observed in the orientation distribution function of the NiTi sheet with respect to Bunge Euler angles (defined in Figure S3) with constant ϕ_2 slices. The two local maxima of orientation density were (1 1 1)[1 $\bar{1}$ 0] and (1 1 1)[0 $\bar{1}$ 1].

S7. Experimental Setups for Mechanical Tension and Fatigue Experiments

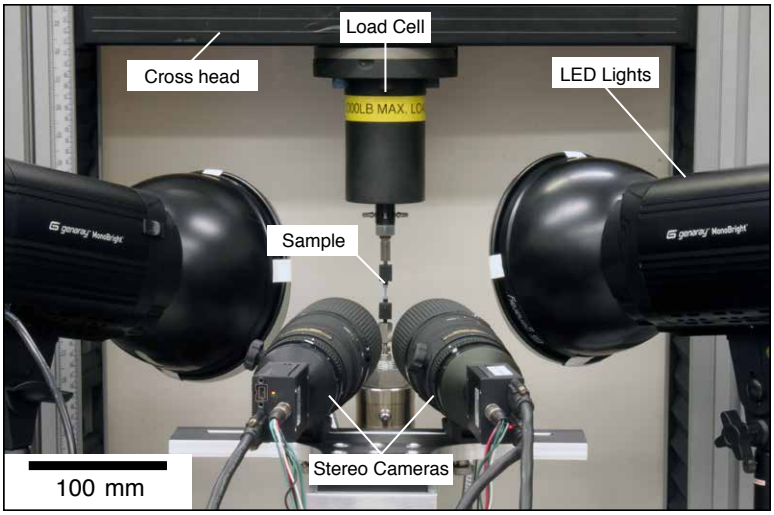

Figure S7: Experimental setup used for the tension experiments described in Sections 2.2.1 and 3.1.

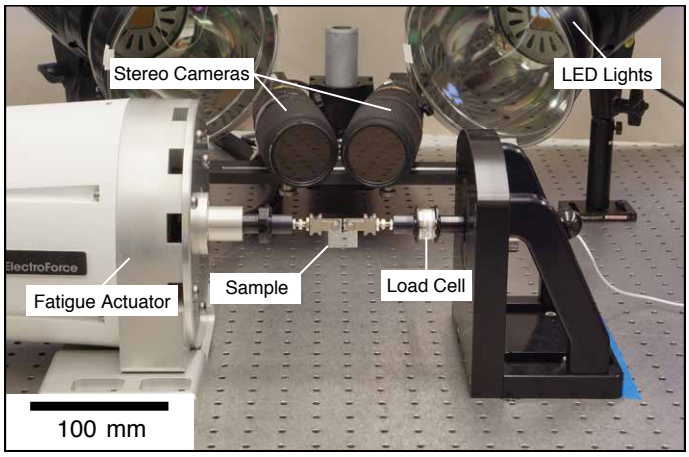

Figure S8: Experimental setup used for fatigue cracking experiments described in Sections 2.2.2 and 3.2.

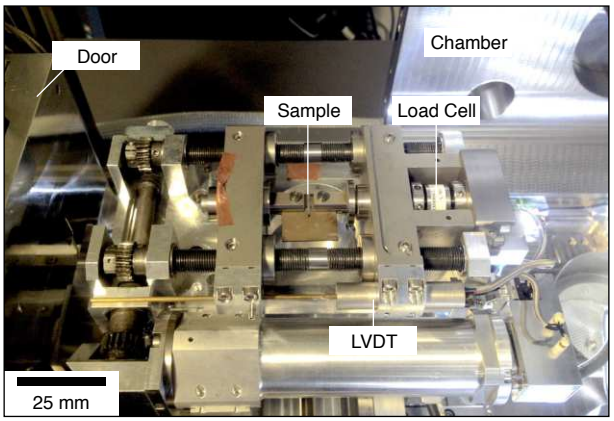

Figure S9: A compact tension sample in the in-situ tension/compression stage for SEM-DIC measurements of the microscale deformation at the crack, described in Sections 2.2.3 and 3.3. The sample was polished to a mirror finish with initially a silver appearance. The orange tinge on the sample is from the relatively large nanoparticles (250 nm) used in the self-assembled Au nanoparticle pattern.

S8. Fitting Constants for Asymptotes

	RD	45	TD
B_1 (GPa)	0.2439	0.2897	0.3164
B_2 (GPa)	-0.1033	-0.0978	-0.0965
B_3 (cycle^{-1})	13.63	11.70	18.84
R^2	0.9871	0.9846	0.9518

Table SI: The fitted terms and coefficients of determination (R^2) for plateau stresses (σ_p) on loading in Figure 3b, following Equation (1). The asymptotes of $n \to \infty$ are the B_1 values.

	RD	45	TD
B_1 (%)	1.145	0.9859	0.4750
B_2 (%)	1.199	1.029	0.4897
B_3 (cycle^{-1})	11.67	10.21	12.40
R^2	0.9976	0.9976	0.9978

Table SII: The fitted terms and coefficients of determination (R^2) for residual strain (ε_r) in Figure 3c, following Equation (1). The asymptotes of $n \to \infty$ are the B_1 values.

S9. Macroscopic Crack Bifurcation

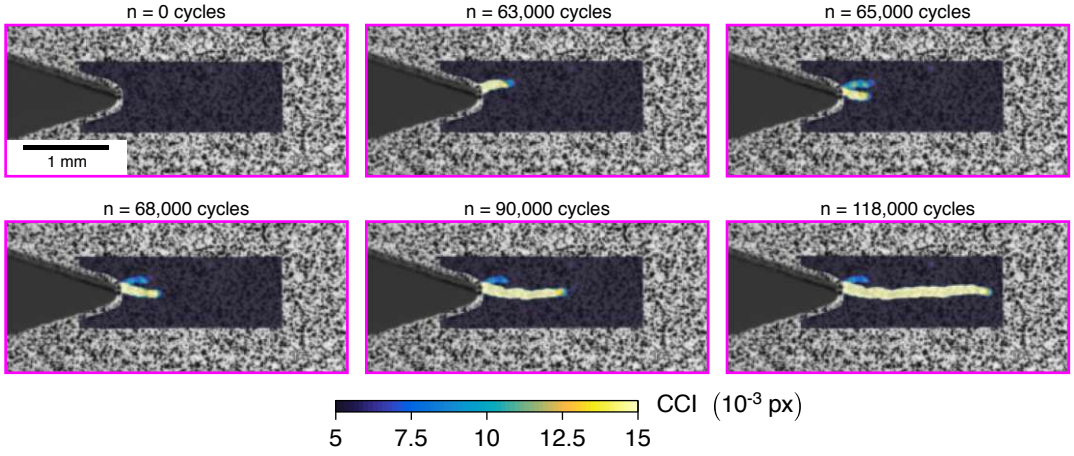

Figure S10: Crack bifurcation was observed in a 45 sample at high ΔK, but not in any of the other samples (albeit, the investigation included a limited number of samples). Due to the bifurcation, the crack growth characteristics of this sample were not compared with the other samples. This underscores the utility of full-field methods like DIC for investigating fatigue crack growth responses.

S10. Fractography with Scanning Electron Microscope (SEM) Images

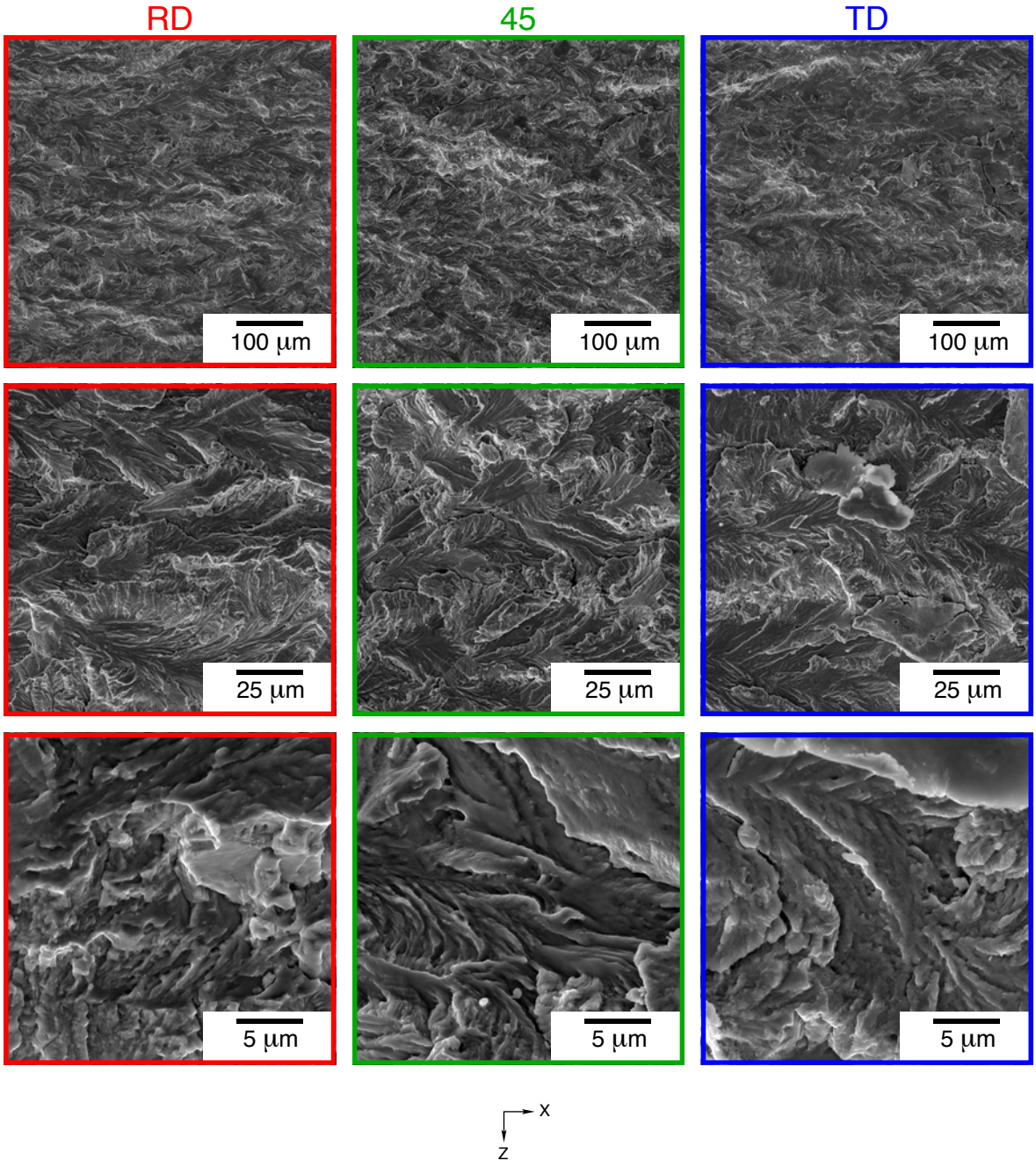

Figure S11: SEM fractography at 1 mm from the notch root (a = 9 mm). The crack growth direction was from left to right, and the images were captured orthogonal to sample surface.

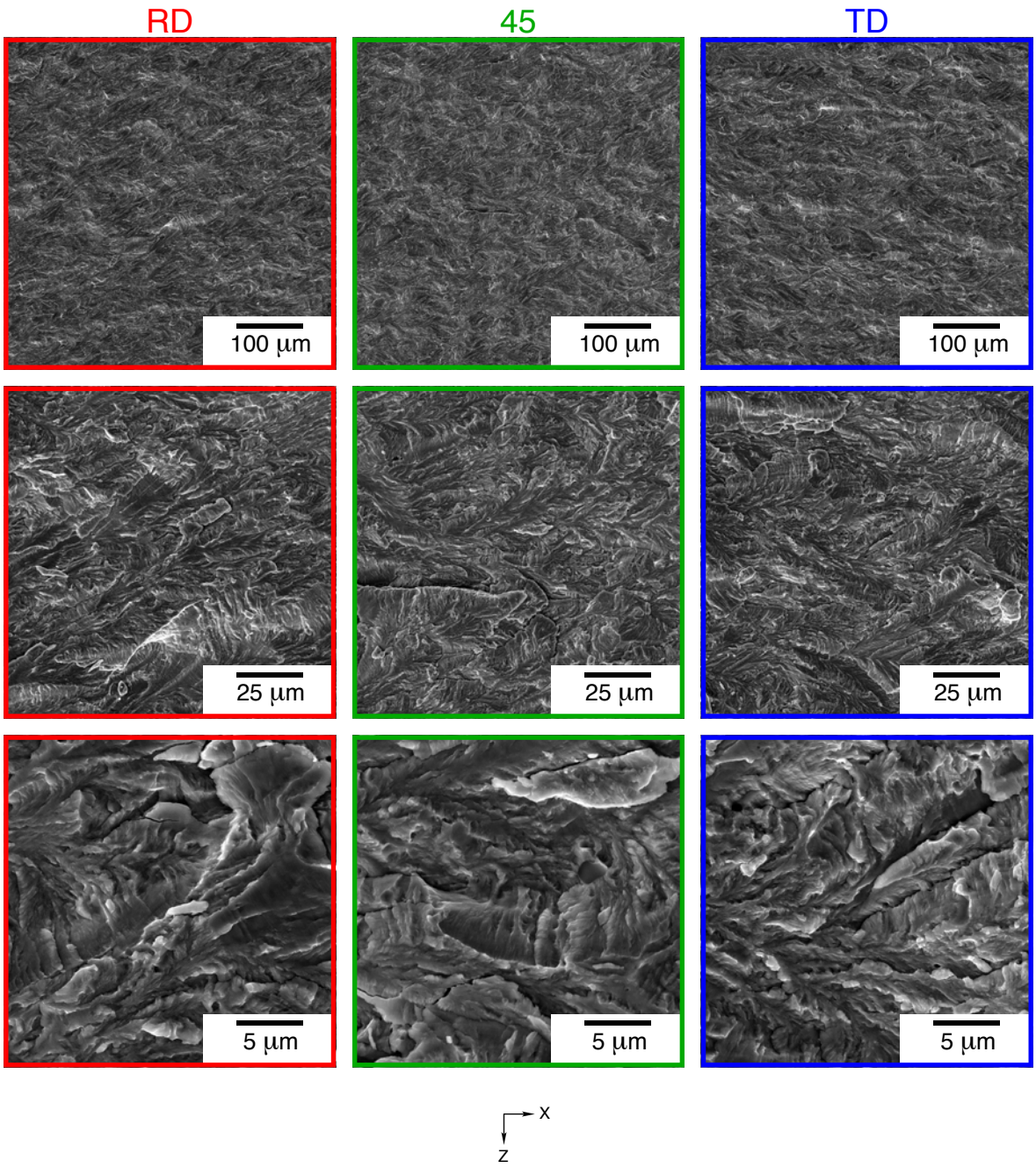

Figure S12: SEM fractography at 4 mm from the notch root (a = 12 mm). The crack growth direction was from left to right, and the images were captured orthogonal to sample surface. No significant differences in roughness were evident, indicating that differences in the fatigue cracking of the RD, 45, and TD samples were not caused by roughness-induced crack closure.